

Multiphase Flow and Granular Mechanics

Ruben Juanes,^{1,*} Yue Meng,¹ and Bauyrzhan K. Primkulov¹

¹Massachusetts Institute of Technology,

77 Massachusetts Avenue, Cambridge, MA, USA

(Dated: October 2, 2020)

Abstract

7 In this perspective we provide a brief overview of the state of knowledge and recent progress in the
8 area of multiphase flow through deformable granular media. We show, with many examples, that
9 the interplay between viscous, capillary and frictional forces at the pore scale determines the mode
10 of fluid invasion. We pay particular attention to the central role of wettability on the morphology
11 of granular-pack deformation and failure. Beyond their intrinsic interest as processes that give
12 rise to spectacular pattern formation, these coupled phenomena in granular media can control
13 continental-scale fluxes like methane venting from the seafloor, and geohazards like earthquakes
14 and landslides. We conclude this perspective by pointing to fundamental knowledge gaps and
15 exciting avenues of research.

16 **INTRODUCTION**

17 The flow of multiple fluid phases through permeable media is key to the understanding,
18 prediction and design of environmental systems, energy resources, climate-change mitigation
19 strategies, and industrial processes. Examples include infiltration of water into the vadose
20 zone [1–4] and resilience of water-limited ecosystems [5–7], contamination (and subsequent
21 remediation) of underground bodies of water by nonaqueous phase liquids [8, 9], geologic
22 CO₂ storage [10–15], hydrocarbon recovery from conventional [16, 17] and unconventional
23 formations [18], methane venting from organic-rich sediments in lakes and the seafloor [19–
24 21], formation and dissociation of methane hydrates in permafrost regions and in ocean
25 sediments [22], water dropout in low-temperature polymer-electrolyte fuel cells [23, 24], and
26 microfluidics towards lab-on-a-chip technology [25–33].

27 The interplay between multiphase flow and granular mechanics controls the morphological
28 patterns, evolution and function of a wide range of systems. For example, it determines the
29 self-assembly of particles and patterning of substrates at the nanoscale [34, 35] [Fig. 1(a)].
30 It is also responsible for the structural integrity of sand castles in moist sand [36] [Fig. 1(b)],
31 “craquelure” in paintings [Fig. 1(c)], and desiccation cracks in clayey soil [37, 38] [Fig. 1(d)]—
32 the latter two phenomena involving a combination of capillarity and shrinkage [39]. The
33 powerful coupling among viscous, capillary and frictional forces can give rise to spectacular
34 patterns, including labyrinths [40] [Fig. 1(e)], corals, and stick-slip bubbles [41]. While the
35 characteristic length scale of these morphologies is typically in the sub-centimeter range,
36 they can determine the mode of gas release in nature at the kilometer scale, as is the
37 case for methane venting from the seafloor [21] [Fig. 1(f)] and volatile gases from volcanic
38 eruptions [42]—thus controlling critical flux exchanges in the Earth’s global biogeochemical
39 cycles.

40 This perspective is aimed at providing a brief overview of the state of knowledge, recent
41 progress, and open questions at the confluence of multiphase hydrodynamics and mechanics
42 of granular systems, with an emphasis on pattern formation. We first address the hydro-
43 dynamic components of the problem, and describe fluid–fluid displacement in rigid porous
44 media. We then extend the description to moveable, deformable and breakable granular me-
45 dia, thus accounting for the coupling between fluid and solid mechanics at the grain scale.
46 We then focus on one particular aspect of this coupling: the role of wettability (the relative

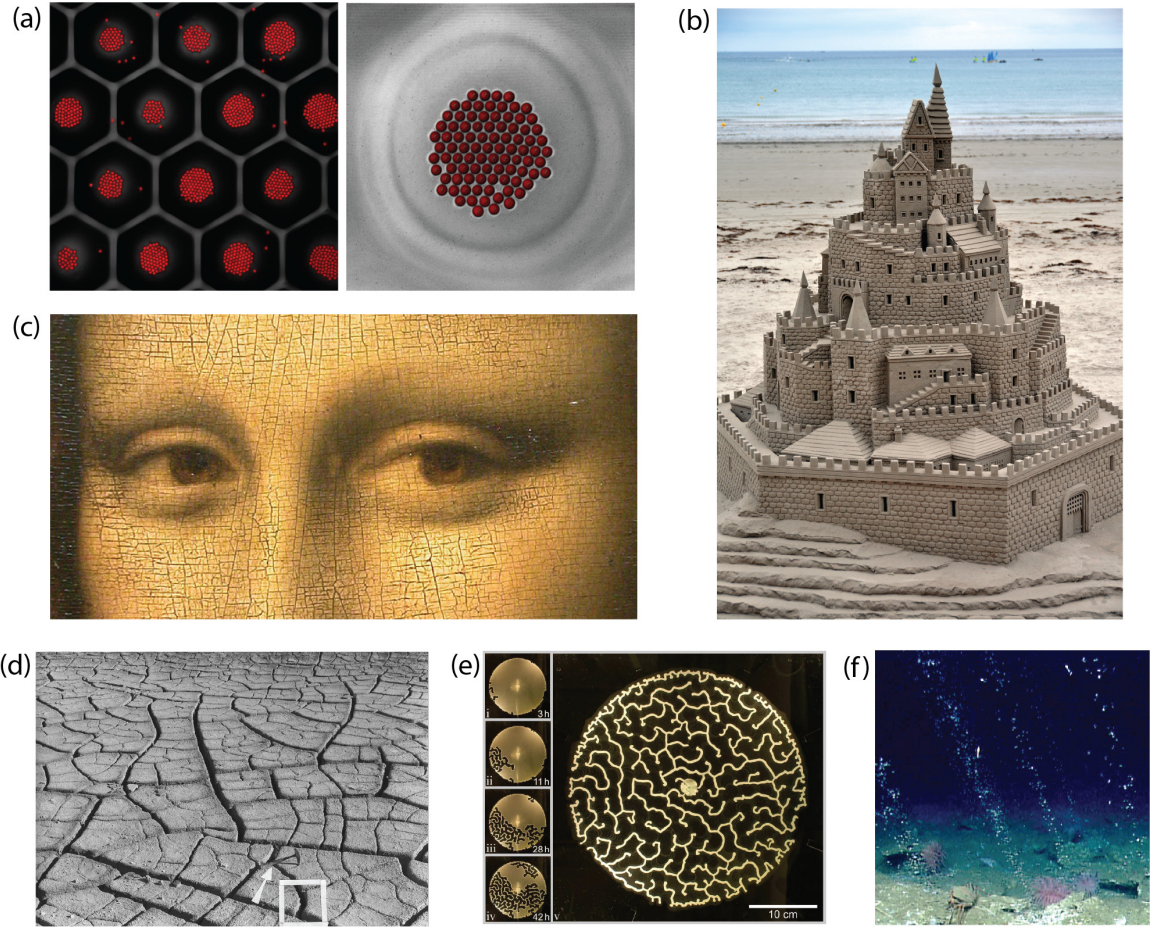


FIG. 1. Visual examples of the powerful interplay between multiphase fluids and the mechanics of granular media. (a) Particle self-assembly at the nanoscale (from Wang *et al.* [35]). (b) Sand castle in moist sand (https://commons.wikimedia.org/wiki/File:Ultimate_Sand_Castle.jpg). (c) Detail of craquelure [art credit: Mona Lisa (La Gioconda) by Leonardo da Vinci]. (d) Desiccation cracks on the soil surface (from Weinberger [43]). (e) Labyrinth patterns formed as a result of air invasion into a frictional suspension (from Sandnes *et al.* [40]). (f) Venting of methane bubbles from the ocean seafloor (from Skarke *et al.* [21]).

⁴⁷ affinity of the solid grains to the different fluids in the pore space) on the morphology of
⁴⁸ granular-pack deformation from fluid injection. Finally, we point to fundamental knowledge
⁴⁹ gaps and exciting avenues of research.

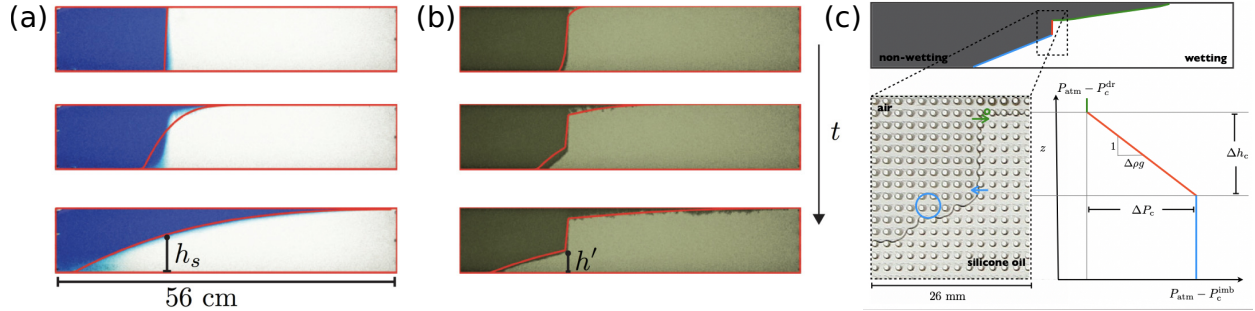


FIG. 2. Lock-exchange flow of (a) miscible and (b) immiscible fluid pair in a glass-bead pack. (c) Fluid–fluid interface pinning in a microfluidic chip. The interface de-pins and moves away from the vertical position only where the local pressure difference between the two fluids is greater than the threshold capillary entry pressure. Adapted from Zhao *et al.* [44].

50 MULTIPHASE FLOW IN RIGID POROUS MEDIA

51 We start by pointing to the fundamentally distinct nature of miscible (single-phase) and
 52 immiscible (multiphase) flow in rigid porous media, which is best done through an example
 53 [44]. Consider a porous medium such as a pack of glass beads filled with two density-
 54 mismatched fluids that share a vertical interface (Fig. 2). The different density of the fluids
 55 drives the lock-exchange flow, where the lighter fluid spreads along the top of the cell. If
 56 the two fluids are miscible, this flow is accompanied by a smooth deformation of the fluid–
 57 fluid front, from vertical towards horizontal [Fig. 2(a)]. In contrast, when the two fluids
 58 are immiscible, a segment of the interface remains indefinitely pinned in its original vertical
 59 configuration [Fig. 2(b)]. In order to fully appreciate the mechanisms responsible for the
 60 striking difference between miscible and immiscible lock-exchange flow in Fig. 2, we need to
 61 define a few concepts.

62 When two fluids are immiscible, the boundary between them is sharp, and interfacial
 63 tension γ pulls along it. This tension is the result of dissimilarity in the molecular interactions
 64 of the two phases [45], which introduces the energy cost per unit area of the interface. As
 65 a result, the system tries to minimize the area of the fluid–fluid interface. In fact, in the
 66 absence of solid surfaces and body forces, the fluid with the smaller volume would roll up
 67 into a sphere. In the presence of a solid phase, the fluid–fluid interface intersects the solid
 68 surface at an angle θ , which we measure within the invading fluid. The contact angle θ is a

69 measure of wettability—it reflects the affinity of the solid to the invading fluid phase. The
70 system is in drainage when $\theta > 90^\circ$, and it is in imbibition when $\theta < 90^\circ$. Furthermore, there
71 is a pressure drop (the Laplace pressure Δp [45]) associated with all fluid–fluid interfaces
72 confined within the pore space. This pressure drop at each interface scales as

73
$$\Delta p \sim \frac{\gamma \cos \theta}{R}, \quad (1)$$

74 where R is the characteristic size of pore throats. Equation (1) anticipates the highest
75 Laplace pressure drop across the invading front when it is in strong drainage ($\theta \rightarrow 180^\circ$)
76 and when it passes through a narrow throat. The interface can get pinned locally if the
77 invading fluid pressure is insufficient to overcome this local threshold capillary pressure.

78 In fact, the local threshold capillary pressures are responsible for the contrasting behavior
79 of miscible and immiscible experiments in Fig. 2: the hydrostatic pressure difference across
80 most of the vertical immiscible interface in Fig. 2(b)-(c) is insufficient to overcome the
81 threshold capillary pressures and squeeze the immiscible interface across local constrictions
82 in either direction. This is responsible for the permanent pinning of the fluid–fluid interface
83 section in its initial vertical position. The fluid–fluid displacement depicted in Fig. 2 is an
84 example of how pore-scale displacement mechanisms can shape the displacement patterns
85 on a macroscopic scale—a hallmark of multiphase flow in porous media.

86 Much of our knowledge of fluid–fluid displacement in porous media was acquired by
87 examining displacement mechanisms at the pore scale [46]. The interplay between pore
88 geometry and the positions of the local interfaces produces distinct pore-scale displacement
89 scenarios, many of which are accompanied by rapid pressure changes [46]. Haines jumps are
90 a prominent example of such pore-scale displacement mechanisms, where the invading fluid
91 experiences a rapid change in curvature (and thus pressure) as it pushes through narrow pore
92 constrictions [47–51]. This mechanism is prevalent in slow drainage, where sudden bursts of
93 the local fluid–fluid interfaces are responsible for sharp fluctuations in the injection pressure
94 signal [52, 53]. In some cases, the speed of the Haines jumps was recorded to be 50 times
95 larger than the mean front velocity [49], and was observed to cascade through tens of pores in
96 a single jump event. Slow fluid–fluid displacement in drainage produces distinct and robust
97 patterns that are faithfully reproduced with invasion-percolation models [54, 55], where the
98 displacement front advances by invading pores with the lowest threshold capillary pressures
99 first. This mode of displacement traps clusters of the defending fluid in two-dimensional

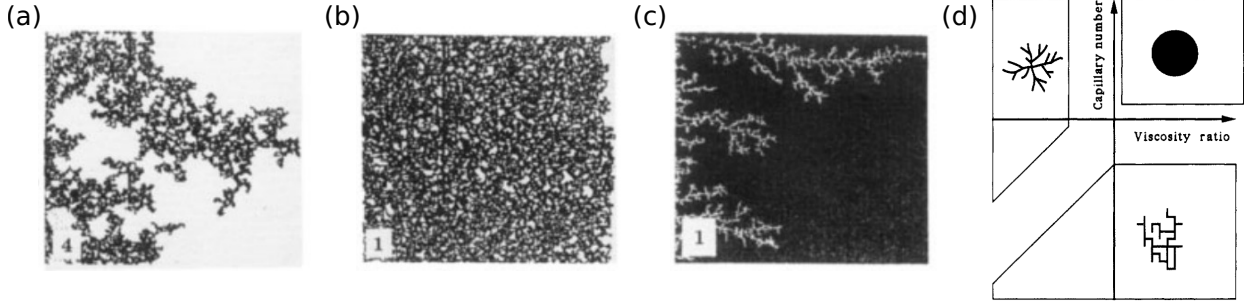


FIG. 3. Lenormand *et al.* [57] studied drainage in porous media and found that the fluid–fluid front can advance through (a) invasion percolation, (b) stable displacement, or (c) viscous fingering, depending on Ca and M . The character of displacement is synthesized in the (d) phase diagram of Lenormand *et al.* [57]. Adapted from Lenormand [58].

100 porous media, producing a self-similar morphology of the invading fluid [56] [Fig. 3(a)].

101 The morphology of the displacement front changes significantly at high injection rates.
 102 When a more viscous fluid displaces a less viscous fluid, it does so through a compact front,
 103 removing most of the defending fluid from the pore space [Fig. 3(b)]. When a less viscous
 104 fluid displaces a more viscous fluid, the invasion front becomes unstable to small perturba-
 105 tions and advances through preferential flow paths [i.e., viscous fingering in Fig. 3(c)]. These
 106 viscous fingering patterns are also self-similar and bear a strong resemblance to diffusion-
 107 limited aggregation patterns [59–61].

108 Our classical understanding of fluid–fluid displacement in drainage has been synthesized
 109 in the seminal diagram of Lenormand *et al.* [57] [Fig. 3(d)]. Here, the character of the
 110 displacement is determined by two dimensionless parameters: the viscosity ratio of the
 111 two fluids $M \equiv \mu_i/\mu_d$, and the ratio of viscous to capillary forces $\text{Ca} \equiv \mu_i u/\gamma$ (capillary
 112 number), where u is the characteristic speed of the displacement front, and μ_i and μ_d are the
 113 invading and defending fluid viscosities, respectively. One can tune the character of fluid–
 114 fluid displacement between viscous fingering, stable displacement, and invasion-percolation
 115 by changing Ca and M . Much of the Ca – M parameter space has been explored with both
 116 experiments [52, 60, 62] and pore-network models [54, 55, 57, 61, 63–73], and although
 117 Lenormand’s phase diagram has been enormously influential and successful in organizing
 118 the current state of knowledge of fluid–fluid displacement in porous media, its applicability
 119 is restricted to systems in strong drainage.

120 There have been sustained efforts towards enhancing our knowledge of fluid–fluid dis-
121 placement to account for wettability effects. A large number of core-scale experiments have
122 shown improved displacement efficiency when the system’s wettability is altered towards im-
123 bibition [74–78]. This was complemented by systematic studies of imbibition under favorable
124 viscosity contrast ($M > 1$) [79–82] and quasi-static pore-network models that accounted for
125 wettability effects [72, 83–88]. More recent efforts have been summarized in Singh *et al.* [89],
126 and include comprehensive studies of wettability effects during fluid–fluid displacement in
127 glass bead packs [90] and microfluidic cells [91], as well as dynamic pore network models
128 that account for wettability effects [73, 92]. Here, we build our discussion around the work
129 of Zhao *et al.* [91] and subsequent numerical efforts of Primkulov *et al.* [72, 73].

130 Zhao *et al.* [91] conducted a series of fluid–fluid displacement experiments in a quasi-
131 two-dimensional porous medium, fabricated with soft lithography techniques by confining
132 a circular post pattern between the two plates of a Hele-Shaw cell. All surfaces of the
133 microfluidic chip were manufactured with a photo-curable resin (NOA 81), where the degree
134 of UV-light exposure is correlated with the surface wettability [93]. Zhao *et al.* [91] filled
135 these wettability-controlled flow cells with viscous silicone oil and injected water from the
136 center at controlled flow rates. The invading fluid patterns in such experiments (Fig. 4)
137 would change depending on Ca and θ , and it is best to describe them alongside the pore-
138 scale mechanisms responsible for the change in patterns.

139 We first traverse the bottom row of experiments in Fig. 4, corresponding to the lowest
140 injection rate and where viscous effects can be neglected. In this limit, the fluid invasion
141 patterns are mainly governed by capillary forces. Cieplak and Robbins [83, 84] defined
142 three pore-scale events that are responsible for advancing the invading fluid front: “burst”,
143 “touch”, and “overlap” (Fig. 5). The “burst” event corresponds to a stable interface that
144 intersects the posts at prescribed θ and has a maximum possible curvature. Increasing the
145 curvature (and therefore Laplace pressure) above the “burst” configuration would render
146 the interface unstable and the invading fluid would occupy the pore space ahead. The
147 “touch” event corresponds to the interface contacting with a nearby post and subsequently
148 occupying the remained of the pore. The “overlap” event takes place when two neighboring
149 menisci overlap on or near a shared post. The “burst” events are prevalent in strong drainage
150 ($\theta = 150^\circ$ in Fig. 4), while “touch” and “overlap” are prevalent near weak imbibition ($\theta = 60^\circ$
151 in Fig. 4): the relative frequency of these pore-scale events is responsible for the transition in

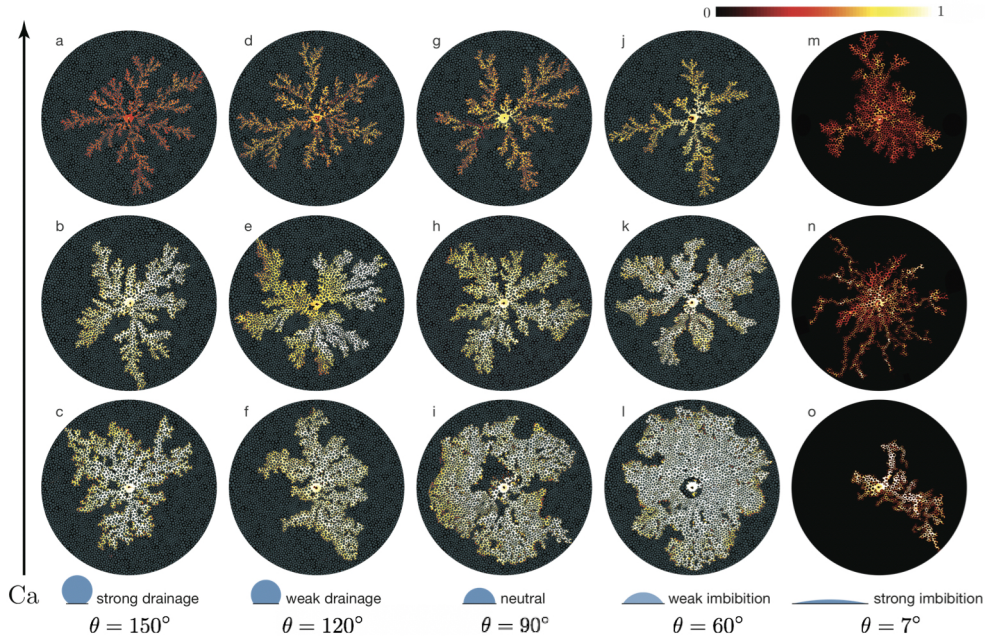


FIG. 4. Water displacing viscous silicone oil in wettability-controlled quasi-two-dimensional porous medium. Water was injected with different Ca under wettability ranging from strong drainage to strong imbibition. The displacement front was shown to advance through invasion percolation, cooperative filling, and corner flow at low Ca. At high Ca water advanced through viscous fingers, either leaving a film of oil or moving through films of water on the solid surfaces. Reprinted from Zhao *et al.* [91].

152 patterns for $60^\circ < \theta < 150^\circ$. In strong drainage, the fluid–fluid displacement is incomplete,
 153 and clusters of the defending fluid are trapped behind the fluid front (Fig. 4, plate C). In
 154 weak imbibition, invading fluid patterns are compact (Fig. 4, plate L). As the wettability
 155 of the solid approaches strong imbibition ($\theta = 7^\circ$ in Fig. 4), the invading fluid no longer
 156 advances by occupying the pores completely. Instead, it advances by coating the corners at
 157 the intersection of posts with top and bottom plates (see “corner flow” in Fig. 5), which
 158 results in patterns equivalent to one on plate O in Fig. 4 [72]. The entire bottom row in Fig. 4
 159 can be modeled as an invasion-percolation model that accounts for arbitrary wettability of
 160 the solid surface by incorporating the four pore-scale events in the quasi-static limit [72].

161 The experiments corresponding to higher values of Ca in Fig. 4 can be modeled by
 162 adding viscous forces to the quasi-static model [72, 73]. Here, it is convenient to draw
 163 an analogy between flow in porous media and currents in an electrical circuit: Poiseuille

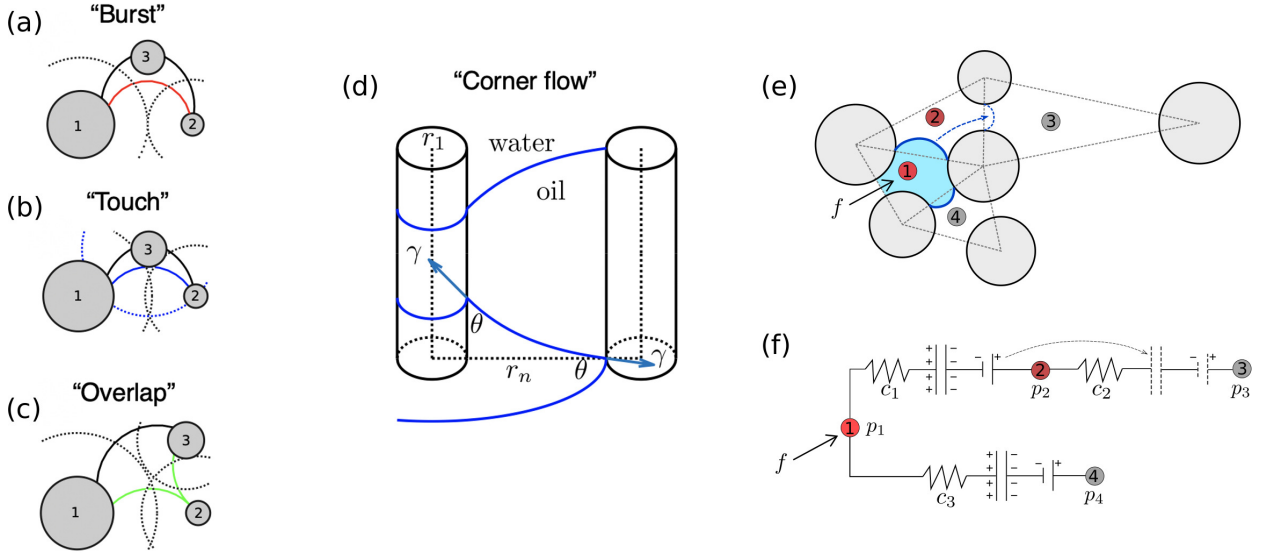


FIG. 5. Pore-scale displacement events that govern quasi-static fluid–fluid flow are (a) burst (i.e. Haines jump), (b) touch, (c) overlap (i.e. coalescence), and (d) corner flow (i.e. coating of posts with wetting fluid). These pore-scale events naturally augment the dynamic pore-network model (“moving-capacitor” model). The “moving-capacitor” model utilizes the analogy between (e) immiscible fluid–fluid displacement in porous media and (f) electrical current, where local fluid–fluid interfaces are represented through capacitors and event capillary entry pressures inform the voltage drop corresponding to dielectric breakdown in a capacitor. Adapted from Primkulov *et al.* [72] and Primkulov *et al.* [94].

flow is equivalent to Ohm’s law, conservation of mass is equivalent to Kirchhoff’s rule, pore channels are represented with resistors, and local menisci are represented with capacitors [73]. In electrical circuits, capacitors experience dielectric breakdown when charges on its plates exceed a threshold value. Analogously, local menisci become unstable and enter a pore whenever the pressure difference across the interface exceeds critical Laplace pressure that corresponds to “burst”, “touch”, or “overlap”. This reduces the two-phase flow problem to a sequence of linear equations, and their solution allows recovering a phase diagram (Fig. 6) that captures the one obtained from experiments (Fig. 4). While our network modeling approach accurately captures the morphology of the invading fluid and its pressure signal over a wide range of $\text{Ca} - M - \theta$ space, it comes with a number of simplifying assumptions (e.g. simplified pore geometry, complete piston-like displacement within individual pore

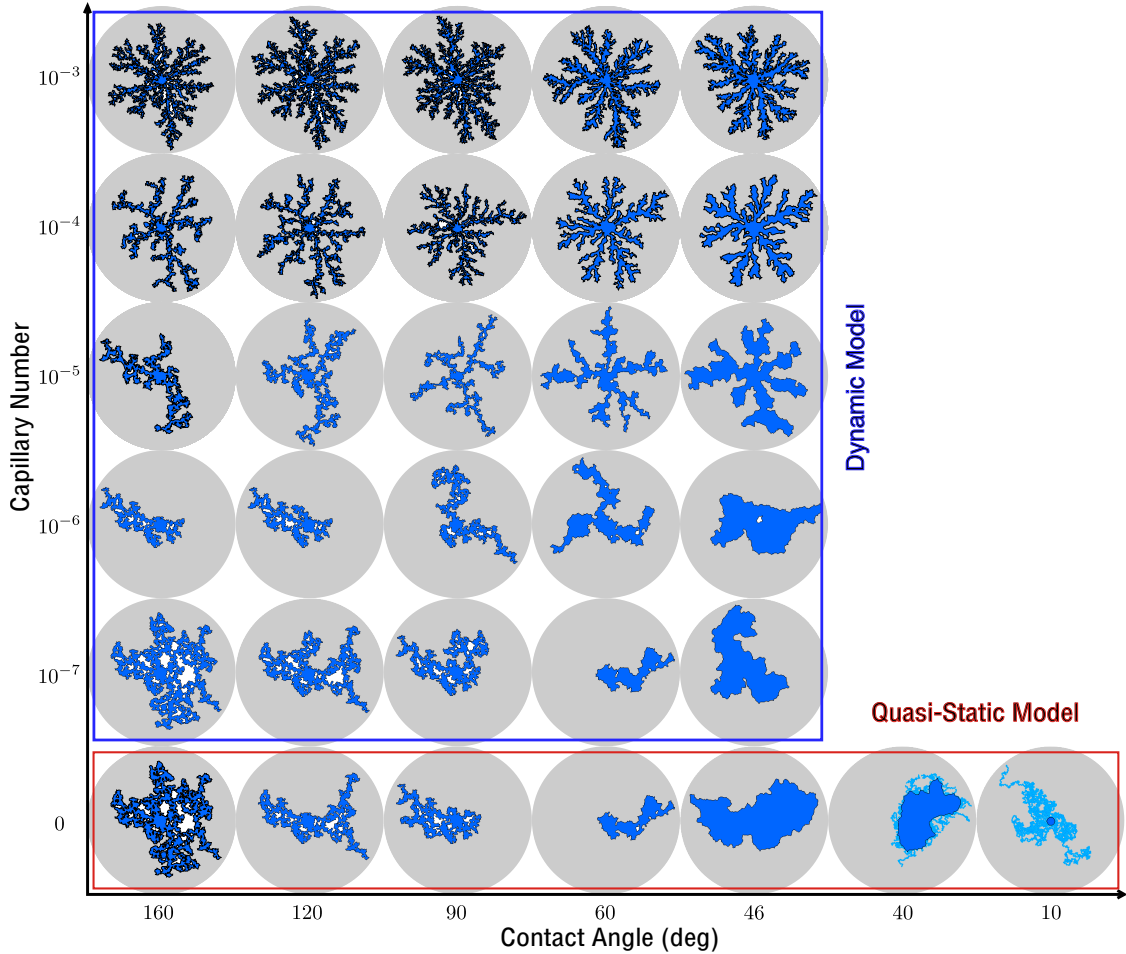


FIG. 6. Numerical simulation of fluid–fluid displacement under different Ca and wettability using quasi-static [72] and dynamic “moving-capacitor” [73] models. The simulations cover the majority of the Ca–M parameter space along with the dominant flow regimes demonstrated in experiments (Fig. 4). Adapted from Primkulov *et al.* [73].

175 throats in all regimes except corner flow) that make it computationally efficient. In fact, the
 176 model has been critically compared with other state-of-the-art pore-scale models [95].

177 MULTIPHASE FLOW IN DEFORMABLE GRANULAR MEDIA

178 When the porous medium is not rigid, there is an interplay between fluid flow and the
 179 mechanics of deformation of the medium. Such interplay is relevant across spatial scales,
 180 from the pore scale [96–100] to the geologic scale [21, 42, 101, 102]. Here, we focus on giving
 181 a brief account of this interplay in granular media, with an emphasis on the grain-scale

182 mechanisms that control pattern formation.

183 The motion of the granular pack can occur in the presence of single-phase flow. For
184 example, groundwater flow can cause the erosion of surface sediments [103], leading to chan-
185 nelization of the flow and incision of river beds in the landscape [104]. Similar physics are
186 responsible for sand mobilization and production from wells in poorly consolidated sedimen-
187 tary rocks [105], whereby cohesion and friction in the granular material are overcome by the
188 hydrodynamic forces that dislodge the contacts and mobilize the grains.

189 Another classic example of medium deformation under single-phase flow is hydraulic
190 fracturing [106], which is typically understood as a result of overcoming the tensile strength
191 of a poroelastic medium upon rapid fluid injection, such that the pore pressure builds faster
192 than it dissipates through the medium [107]. In the context of fine-grained media like
193 clay slurries and colloidal suspensions, Van Damme *et al.* [108], Lemaire *et al.* [109] first
194 identified that a (viscoelastic) fracturing regime could be reached as a transition from the
195 viscous fingering regime. This transition was strongly controlled by the Deborah number,
196 De , where for $De \ll 1$ viscous effect dominate, whereas for $De \gg 1$ the system behaves as an
197 elastic solid. A recent study on a system of a 2D monolayer of elastic frictionless hydrogel
198 particles showcased inelastic deformation, resulting in the formation of an injection cavity
199 from the collective rearrangement of the particles [110].

200 Here we are interested in *multiphase* fluid systems, where two or more fluid phases co-
201 flow through the granular medium. The fundamental notion in extending the description of
202 multiphase flow in rigid porous media is that one must account for the possibility that the
203 grains may move as a result of the fluid–fluid displacement (Fig. 7). This picture at the grain
204 scale makes it apparent that surface-tension forces need to be invoked in the description of
205 the system’s evolution [38, 40, 96, 100, 111–113].

206 **Gas venting**

207 An area that has received substantial attention is the migration of gas within (and sub-
208 sequent release out of) soft, organic-rich, aquatic sediments [19–21]. From a geoscience
209 perspective, this problem is central to understanding methane fluxes and the global carbon
210 cycle, including its dependence on, and feedback to, climate change [22]. There is by now
211 indisputable direct evidence of widespread methane venting from the seafloor [19, 21, 114–

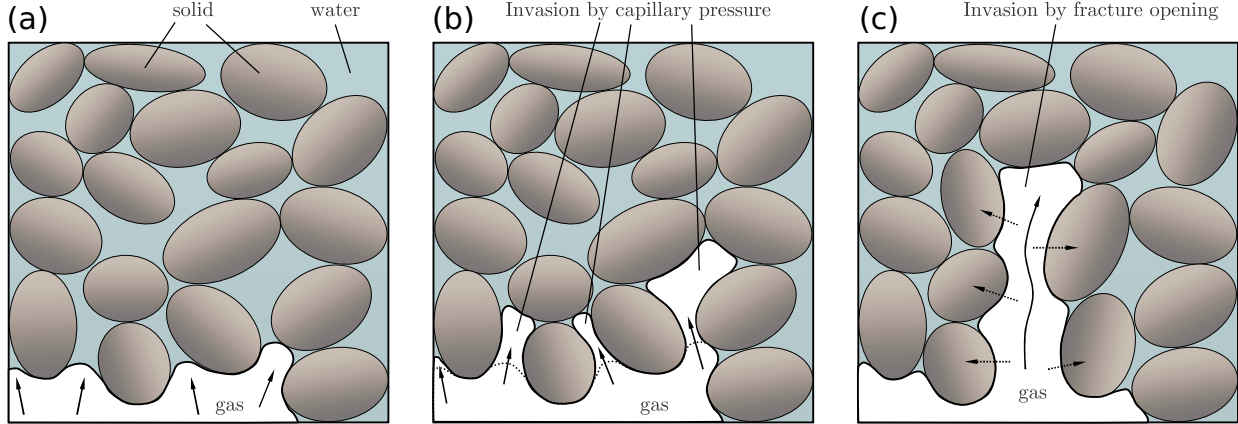


FIG. 7. Schematic diagram of the two modes of fluid–fluid displacement (gas–water) in a deformable granular medium. (a) The fluid–fluid interface before displacement. (b) Fluid invasion when the medium behaves rigidly. (c) Invasion by conduit opening; the exerted fluid pressure is sufficient to overcome confinement, cohesion and friction at grain contacts. Reprinted from Jain and Juanes [111].

118], shallow and deep lake sediments [20, 119–123] and man-made reservoirs [124]. This
 213 concept of conduit opening in unconsolidated sediments has also been invoked to explain
 214 gas migration at geologic spatial and time scales [101, 102, 125, 126].

215 To explain these phenomena, several groups have conducted controlled laboratory ex-
 216 periments of vertical gas migration in unconsolidated granular materials, almost exclusively
 217 in 2D or quasi-2D systems (a Hele-Shaw cell packed with beads or grains). These studies
 218 have led to direct observations of the morphology of air invasion, delineating conditions un-
 219 der which the granular pack behaves rigidly or opens conduits for gas migration [127–130].
 220 In particular, the mode of invasion can transition from fingering to fracturing during the
 221 course of a single experiment, as the gas (injected at the bottom of the cell) migrates up-
 222 wards to regions of the granular pack subject to lower confining stress [131]. In soft systems,
 223 the interplay between elasticity, confinement and buoyancy can lead to a range of mixed
 224 gas-migration regimes, and the emergence of episodic capture-venting dynamics [132].

225 Some 3D experimental systems have investigated the surface footprint of venting dynam-
 226 ics, either from point gas injection in granular media [133] or from actual *in situ* methane gen-
 227 eration in lake-mud incubation experiments [134]. Only recently have experimental studies
 228 addressed the 3D dynamics of vertical gas migration in deformable granular media through

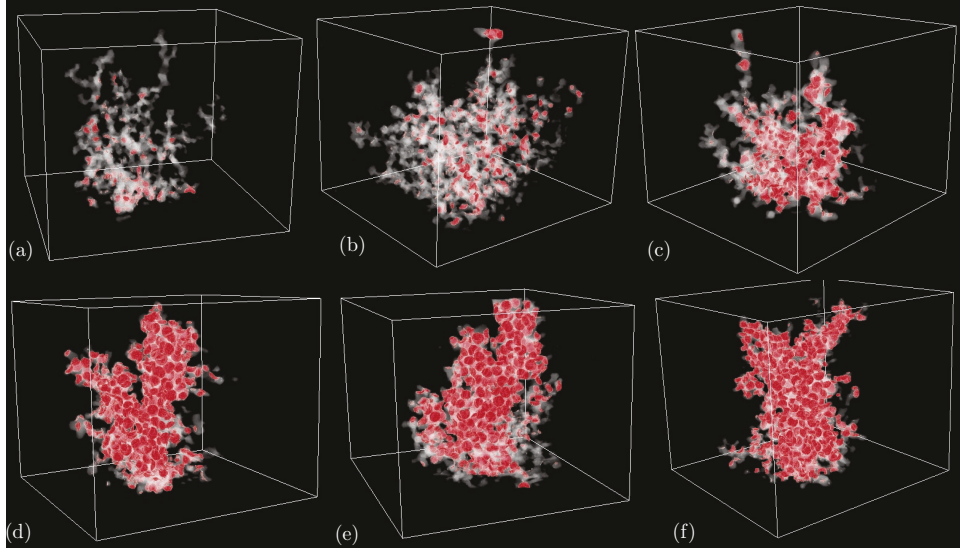


FIG. 8. 3D PLIF reconstructions of the fluid invasion pattern (in white) superimposed on the conduit opening (in red) for experiments in which a fluid (silicon oil) is injected at the bottom of a pack of glass beads to displace a more viscous fluid (glycerol). Reprinted from Dalbe and Juanes [136].

229 direct visualization. Sun and Santamarina [135] employed fumed silica and a refractive-
 230 index-matching oil blend, and two orthogonal camera views for partial 3D characterization
 231 of the gas migration process. Dalbe and Juanes [136] developed an experimental setup
 232 to fully reconstruct the coupled invasion-deformation dynamics in 3D. They constructed a
 233 porous cell made of borosilicate glass beads, filled it with glycerol to achieve refractive-index
 234 matching, and injected less-viscous silicon oil that is also index-matched. They employed
 235 a planar laser-induced fluorescence (PLIF) technique in which a laser sheet, mounted on a
 236 moving stage, shines on the medium and excites fluorescent dyes premixed with the defend-
 237 ing and invading fluids. This technique allowed them to reconstruct the 3D dynamics of the
 238 granular pack at the subpore scale (Figure 8).

239 **Desiccation cracks**

240 The phenomenon of desiccation cracks is a common occurrence in drying soil [43, 137]
 241 and paint [138, 139], often leading to polygonal patterns [140] [Fig. 1(c)-(d)]. Controlled lab
 242 experiments on monolayer packings [97, 98], colloidal suspensions [141–143] and soil systems

[37, 137, 144] have paved the way for improved understanding and modeling at the particle level [38, 97, 98, 145–148] and, recently, at the continuum level using phase-field models [149, 150].

This cumulative understanding has elucidated the critical role of capillary forces in the initiation and propagation of cracks [38], and the dominant control of shrinkage in determining the characteristic size of the cracked patterns—something that has recently been demonstrated with an analogue hydrogel model, where the individual particles undergo shrinkage and swelling [39, 151].

Frictional flows

The morphology of fluid invasion and granular deformation is ultimately determined by the interplay among viscous forces, capillary forces and interparticle forces. Interparticle forces can have different origins, including cementation and cohesion at particle contacts that lead to tensile strength, and friction between particles, which depends strongly on the grain material, particle roughness and degree of confinement—itself a function of packing fraction and confining stress.

This interplay was studied in depth in a series of investigations of so-called “frictional flows” [40, 41]. In this experimental setup, air is injected to displace a layer of beads submerged in a defending fluid within a Hele-Shaw cell [Fig. 9(a)]. As the layer of beads is displaced, beads accumulate at the air–fluid interface, forming a front of dense bead-pack ahead of the interface [Fig. 9b]. The air injection rate controls the balance between viscous and capillary forces, and the initial packing fraction of the suspension controls the degree of confinement. At a given packing fraction, low injection rates result in “frictional” invasion, characterized by frictional fingers or stick-slip bubbles. For the same packing fraction, as the injection rate increases, there is a transition in invasion morphology to one dominated by a fluidized front and coral-like patterns and, ultimately, to the classic Saffman–Taylor finger in viscous fluids [152] [Fig. 9(c)]. The invasion patterns and dynamics are also affected by the compressibility of the system [41, 153] and the presence of a gravitational potential [154].

Of particular interest is what happens as the packing fraction increases, that is, as the system moves from a loose segregated suspension to a dense granular pack. The inva-

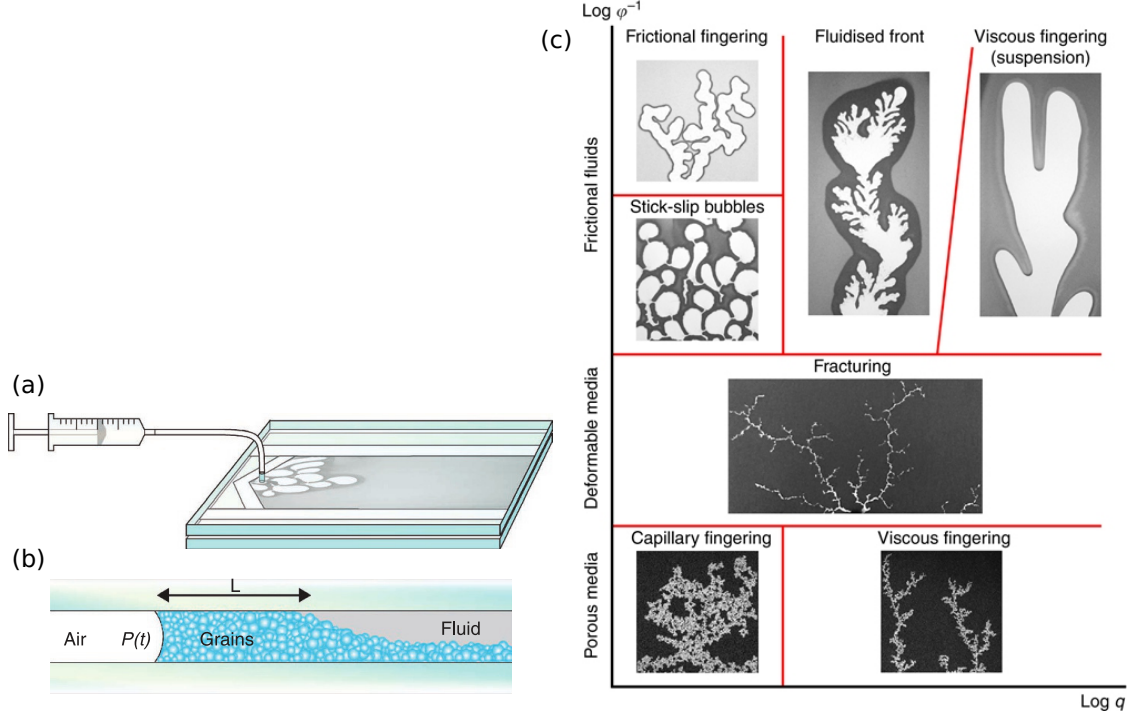


FIG. 9. Schematic of the experimental setup for frictional flows; (a) air is injected into a Hele-Shaw cell loaded with polydisperse glass beads that have settled in a water/glycerol solution; (b) the invading air/fluid interface accumulates a front of close-packed grains in the gap between the plates. (c) Phase diagram of frictional-flow morphologies in the space of injection rate (increasing to the right) and packing density (decreasing to the top). Reprinted from Sandnes *et al.* [41].

sion pattern then undergoes another transition, from frictional flow to fracturing, and from fracturing to fluid–fluid displacement in a rigid medium [Fig. 9(c)]. To quantitatively understand this morphological transition, Holtzman *et al.* [112] conducted experiments of air invasion into a Hele-Shaw cell with a liquid-saturated granular pack, in which the degree of confinement was controlled not by the packing fraction but, rather, by the confining stress [Fig. 10(a)]. At sufficiently high confining stress, the granular pack behaves as a rigid porous medium. The morphology of air invasion is then determined by the capillary number Ca , and exhibits a transition from capillary fingering to viscous fingering. This transition occurs when the characteristic macroscopic viscous pressure drop in the direction parallel to flow, δp_v is balanced with the variation in capillary entry pressures along the interface, δp_c . The

283 condition $\delta p_v \sim \delta p_c$ is controlled by a “modified capillary number” [112, 155, 156]:

284

$$\text{Ca}^* = \underbrace{\frac{\eta(Q/bd)}{\gamma}}_{\text{Ca}} \frac{R}{d}, \quad (2)$$

285 where Ca is the classic capillary number [57], Q is the injection rate, b is the height of the
286 cell, d is the grain size, and R is the cell radius.

287 As the confining stress decreases, the granular pack loses its rigidity and is subject to
288 grain motion concomitant with fluid invasion. In a granular medium, conduits open when
289 forces exerted by the fluids exceed the mechanical forces that resist particle rearrangements.
290 In cohesionless granular material, these forces include elastic compression and friction. For
291 systems with densely packed, highly compliant frictionless particles, conduit opening is con-
292 trolled by particle deformation [132]. However, for many types of particles including most
293 mineral grains and manufactured beads, the high particle stiffness limits interparticle com-
294 pression, making frictional sliding the dominant deformation mechanism that alters the pore
295 geometry [112, 157].

296 The emergence of fracturing is determined by the so-called “fracturing number”, N_f , that
297 measures the system deformability as the ratio of the pressure forces that drive fracturing
298 (capillary pressure γ/d and local viscous pressure drop, $\nabla p_v d \sim \eta v/d$) and the resisting
299 force due to friction [112]:

300

$$N_f = \frac{(\gamma/d)(1 + \text{Ca})}{\mu\sigma'}, \quad (3)$$

301 where μ is the coefficient of friction, and $\sigma' \sim W/R^2$ is the effective confining stress, with
302 W the weight on top of the cell.

303 Indeed, the two transitions are observed experimentally: from capillary fingering to vis-
304 cous fingering at $\text{Ca}^* \sim 1$ at high confining stresses, and from either capillary fingering or
305 viscous fingering to fracturing at $N_f \sim 1$ (Fig. 10). While the transition to fracturing from
306 viscous pressure drop is relatively well understood, and the basis for hydraulic fracturing
307 [106, 107], the work of Holtzman *et al.* [112] demonstrates that the transition to a granular
308 fracturing regime can occur as *capillary fracturing*, at vanishing flow rates.

309 IMPACT OF WETTABILITY ON FRICTIONAL FLOWS

310 Given the wealth of evidence demonstrating the importance of capillarity on deformation
311 and fracture of granular media [41, 112, 157–159], the fundamental question that arises and

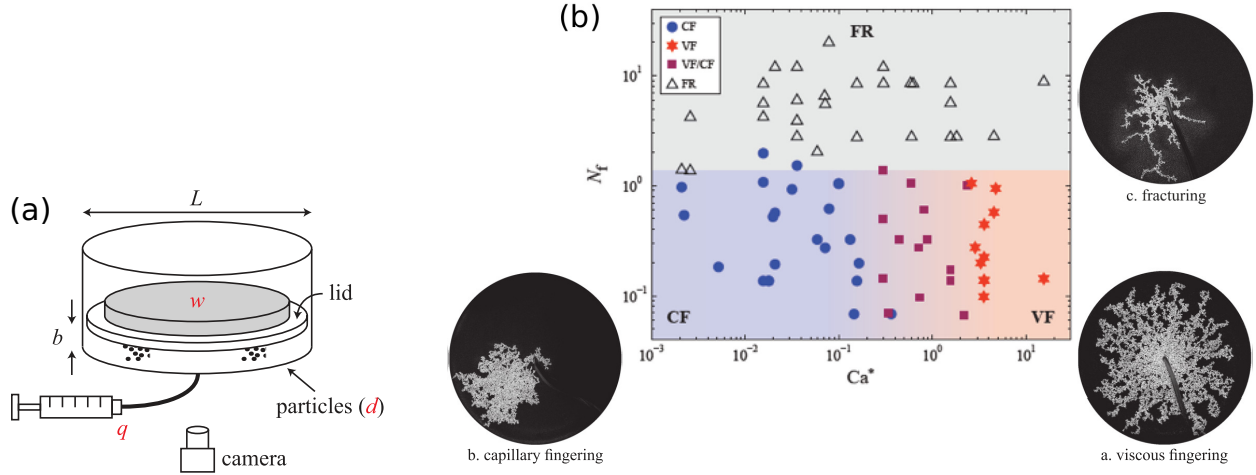


FIG. 10. (a) Experimental setup of hydrocapillary fracturing experiments, where a thin bed of water-saturated glass beads is confined in a cylindrical acrylic cell, subject to a weight placed on a disk that rests on top of the beads. Air is injected into the center of the cell at a fixed flow rate. (b) Phase diagram of drainage in granular media, showing three invasion regimes: viscous fingering (VF), capillary fingering (CF), and fracturing (FR). The tendency to fracture is characterized by the “fracturing number” N_f : drainage is dominated by fracturing in systems with $N_f \gg 1$. At lower N_f values, the type of fingering depends on the modified capillary number, Ca^* . Adapted from Holtzman *et al.* [112].

312 has remained unexplored until very recently is how wetting properties impact the emergence
313 of granular fracture, and the ensuing fracture pattern.

To investigate the impact of wetting on fracturing of granular media, Trojer *et al.* [160] used an experimental setup similar to that of Holtzman *et al.* [112]—in which a low-viscosity fluid is injected into a circular Hele-Shaw cell filled with a dense glass-bead pack that is saturated with a more viscous, immiscible fluid—but now carefully tailoring the wettability of the fluid pair to the glass. The key result is a comparison of the fluid invasion patterns that develop for different wettability conditions (Fig. 11). The results demonstrate that the fracture morphology exhibits a non-monotonic dependence on wettability: highly ramified, disconnected, and ephemeral fracturing in drainage (Fig. 11, left); robust, hierarchical and persistent fracturing in weak imbibition (Fig. 11, center); and no fracturing in strong imbibition (Fig. 11, right). The physical mechanism responsible for the striking differences in the fracture morphology is a transition in the pore-scale fluid displacement from pore-invasion

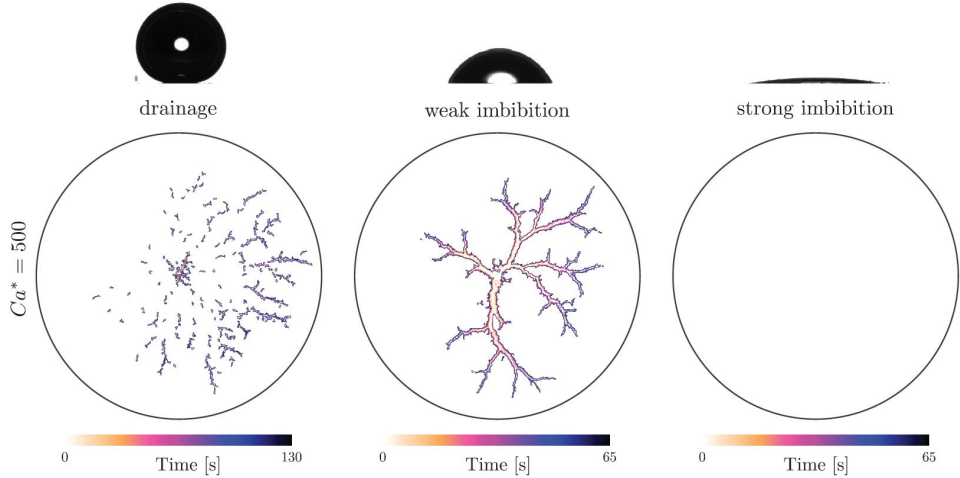


FIG. 11. Comparison of fracture networks that develop for different wettability conditions (strong drainage, weak imbibition, and strong imbibition), under the same modified capillary number and confining stress. Shown are the contours of the evolving fracture patterns at different times during injection (see colormap). Adapted from Trojer *et al.* [160].

325 in drainage, to cooperative filling in weak imbibition, to corner flow in strong imbibition.
 326 These experimental observations indicate that wettability plays a fundamental role in
 327 fracturing of granular media, even at high capillary numbers when viscous forces dominate.
 328 In an effort to understand this behavior, Meng *et al.* [161] developed a fully-coupled dy-
 329 namic model of multiphase flow and granular mechanics at the grain scale. The fluid–fluid
 330 displacement is simulated by the “moving capacitor” dynamic network model described ear-
 331 lier [73], which explicitly incorporates the impact of wettability. The dynamic flow network
 332 model is coupled with a discrete element model (DEM) [162], which simulates the mechanics
 333 of the granular pack by solving the linear and angular momentum balance equations of the
 334 many-body system with appropriate frictional–elastic interaction laws at the interparticle
 335 contacts [163]. To capture the two-way hydromechanical coupling, the pore-pressure forces
 336 are applied to the particles, leading to deformation and rearrangement, and particle motions
 337 feed back into pressure calculations by changing the pore-network geometry and topology.
 338 Meng *et al.* [161] simulated the injection of a less viscous fluid into a frictional granu-
 339 lar pack initially saturated with a more viscous, immiscible fluid, at an injection rate slow
 340 enough that viscous pressure gradients are dissipated between front movements, and cap-
 341 illary effects govern the displacement [53]. The simulations show that fluid invasion first

342 occurs by the expansion of a cavity, followed by fracturing [Fig. 12(b)].

343 Remarkably, they also show that a decrease in θ —that is, transitioning from drainage to
344 weak imbibition—leads to an earlier onset of fracturing, as evidenced by the smaller size of
345 the fluid cavity [Fig. 12(b)]. This behavior cannot be explained by the evolving injection
346 pressure level, or the evolving packing fraction outside the cavity, or the volume of fluid
347 injected alone. Indeed, the transition to fracturing for different wetting conditions occurs at
348 different injection pressures, packing fractions and injected volumes [161].

349 To rationalize this behavior, Meng *et al.* [161] hypothesized that the emergence of frac-
350 turing is akin to a phase transition from liquid-like to solid-like behavior, and, thus, that
351 it can be understood as a *jamming transition*. The classic metrics that characterize the
352 jamming transition in dry granular media [164, 165], such as the mean particle stress P
353 rising from a near-zero background as a function of the evolving mean packing fraction ϕ ,
354 can be used to determine the critical packing fraction ϕ_c at which the jamming transition
355 occurs [Fig. 12(a), inset]. This transition point from the jamming analysis agrees with the
356 simulation results, which show that granular-pack deformation after jamming occurs almost
357 exclusively by fracturing [Fig. 12(b)].

358 The coupled multiphase flow–mechanics grain-scale model was used to explore the rich
359 emerging behavior as a function of two parameters, the contact angle θ varying from 140°
360 (drainage) to 46° (imbibition), and the initial packing density ϕ_0 varying from 0.68 (loose
361 pack) to 0.84 (dense pack). Figure 13 depicts the distinct morphological regimes that arise
362 from injection as a visual phase diagram for different values of θ and ϕ_0 . The patterns are
363 categorized into four different regimes: (I) cavity expansion and fracturing, (II) frictional
364 fingers, (III) capillary invasion, and (IV) capillary compaction. The system’s response,
365 and the transitions among the different regimes, can be synthesized in the form of a phase
366 diagram of jamming in wet granular media [161], which extends its classic counterpart for
367 dry granular systems [166].

368 OUTLOOK

369 Although much progress has been achieved in accounting for wettability effects with
370 dynamic pore-network models in rigid porous media, many challenges still remain. The
371 state-of-the-art dynamic pore network models are limited to system wettabilities between

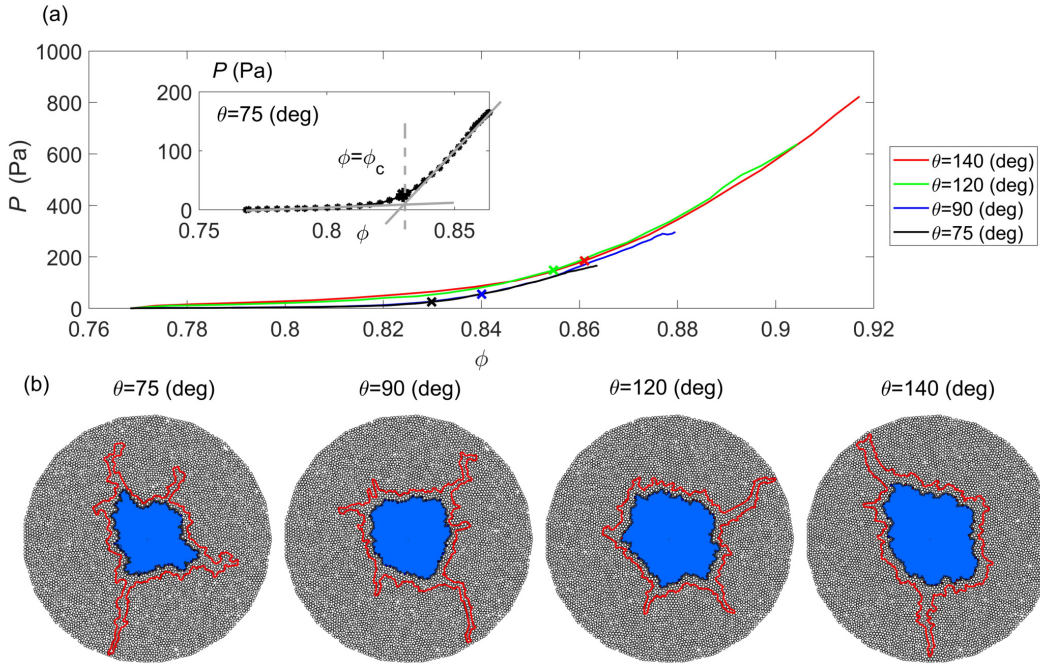


FIG. 12. Jamming transition analysis for the same injection rate and initial packing fraction ($\phi_0 = 0.77$), and four different wetting conditions ranging from weak imbibition to drainage: $\theta = 75^\circ, 90^\circ, 120^\circ, 140^\circ$. (a) Mean particle stress P as a function of packing density ϕ in the compacting granular layer. Inset: determination of the critical packing fraction at jamming, ϕ_c , for $\theta = 75^\circ$; (b) Interface morphology at the jamming transition identified from (a) (black line), compared with that at breakthrough—when the invading fluid first reaches the outer boundary (red line). The comparison confirms that the jamming transition determines the onset of fracturing, and that this transition occurs earlier in imbibition ($\theta = 75^\circ$) than in drainage ($\theta = 140^\circ$). Adapted from Meng *et al.* [161].

372 strong drainage and weak imbibition [73, 95]. With this knowledge, however, it should be
 373 possible to update Lenormand's Ca– M diagram for drainage [57] [Fig. 3(d)], and account
 374 for wettability with contact angle θ as a third axis [94]. From a modeling standpoint, the
 375 strong imbibition regime in porous media has, so far, only been explored with a quasi-static
 376 model [72], and it would be interesting to extend this to a dynamic description.

377 Existing dynamic pore-network models that are able to account for wettability [73, 92]
 378 do so for the paradigmatic case of cylindrical obstacles confined between two plates of Hele-
 379 Shaw cells [83, 84, 91]. As the next step, one could extend these models to a monolayer

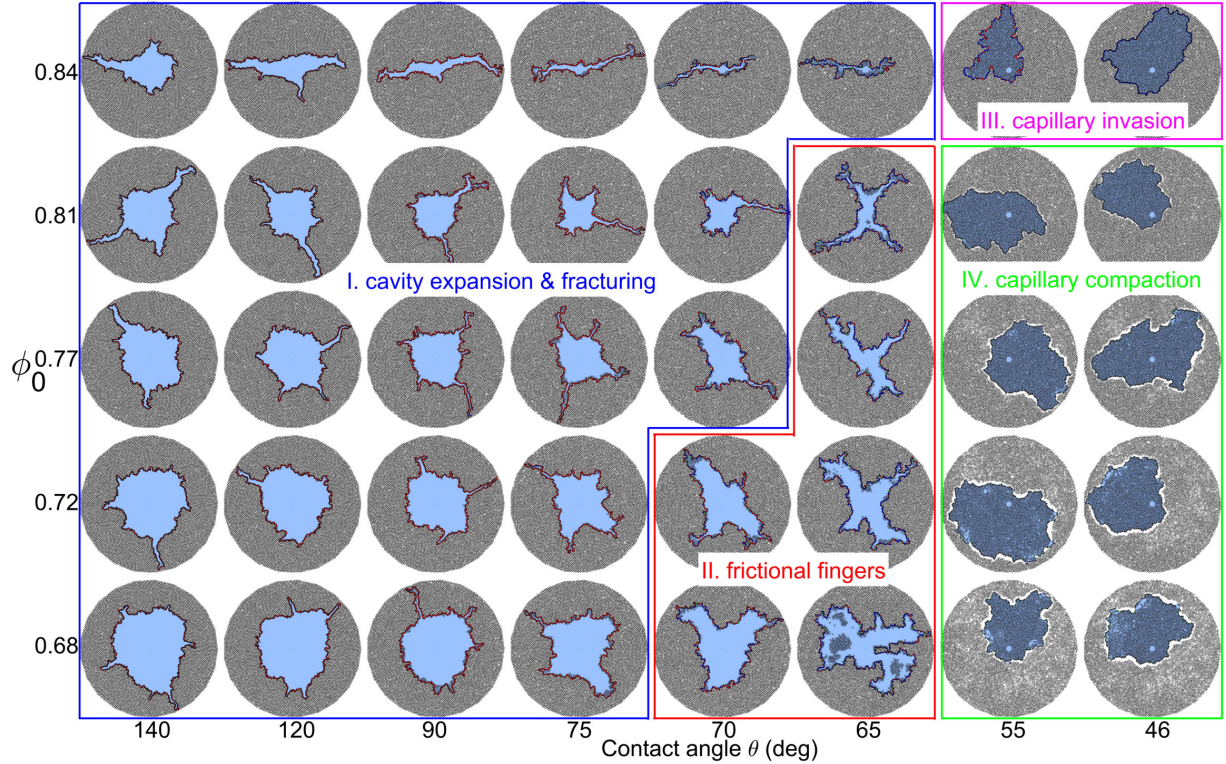


FIG. 13. Visual phase diagram of the invading fluid morphology at breakthrough corresponding to different substrate wettabilities (contact angle θ) and initial packing densities ϕ_0 . Four distinct morphological regimes are identified: (I) cavity expansion and fracturing, (II) frictional fingers, (III) capillary invasion, and (IV) capillary compaction. Reprinted from Meng *et al.* [161].

380 configuration, similar to the one used in many experiments [39, 52, 53, 60, 110, 167]. Even-
 381 tually, the quasi-static models that account for wettability [72, 83, 84] should be extended
 382 to three-dimensional bead packs, and augmented to incorporate dynamic effects [73]. These
 383 efforts would yield important insights into the grain-scale mechanisms at play [161] in actual
 384 3D systems.

385 From an experimental standpoint, the strong imbibition regime has been studied only
 386 under a very limited set of conditions [91, 168], and much of the Ca–M parameter space
 387 in this regime is yet to be systematically explored. In particular, it would be interesting to
 388 study the statistics of invasion avalanches in the coating of posts at low Ca, and characterize
 389 the universality class of this fluid–fluid displacement regime. Another important question
 390 pertaining to fluid–fluid displacement in rigid porous media is the post-breakthrough be-
 391 havior, that is, the evolution of fluid occupancy *after* the invading fluid has reached the

392 outlet—a process of direct relevance to hydrocarbon recovery and non-aqueous phase liquid
393 (NAPL) remediation, but which has only recently started to be investigated [e.g., 168].

394 A frontier in the experimental investigation of the interplay between fluid and solid me-
395 chanics of granular media is the ability to directly characterize the evolution of stresses.
396 While following the deformation of the granular pack with particle tracking or digital image
397 correlation [157, 160] may allow *inferring* the stress field at the particle scale [169–171], no
398 experimental system has so far permitted direct visualization of the interparticle forces in
399 granular packs subject to fluid injection and pore pressure variations. To experimentally
400 visualize stresses in coupled granular–fluid systems, photoelasticity is a promising technique.
401 Photoelasticity has been used as an experimental technique to quantify the internal stresses
402 within solid bodies for decades [172], and it provides a wealth of microscopic observables in
403 assemblies of cylindrical disks, including contact forces [173, 174], length and orientation of
404 force chains [175], particle coordination number [176] and stick-slip behavior [177], that are
405 vital for gaining a deeper understanding of the macroscopic behavior of granular systems.
406 It would be enormously useful to extend this technique to poromechanical granular systems
407 that, contrary to assemblies of cylindrical disks, have a connected pore space through which
408 fluid can flow and fluid–fluid interfaces can move.

409 Finally, the frictional response of pore–granular media plays a central role in geohaz-
410 ards like landslides [178, 179] and earthquakes [180, 181]. There is a need for continuing
411 to advance our fundamental understanding of the frictional behavior of granular material
412 [182] under fluid pressurization [183–188] and in the presence of multiphase fluids, and
413 to develop improved constitutive models [189, 190] that honor the microscale physics and
414 capture the seismic–aseismic transitions in friction. This knowledge would elicit intriguing
415 questions for prediction of geohazards, including whether it is possible to find precursors—
416 such as microtremors—to the onset of catastrophic failure in landslides [179] and, conversely,
417 precursors—such as creep aseismic deformation—to the onset of seismic, runaway-slip failure
418 in earthquakes [187, 191].

419 ACKNOWLEDGMENTS

420 This work was supported by the US Department of Energy (grant DE-SC0018357) and
421 the US National Science Foundation (award CMMI-1933416).

422 * juanes@mit.edu

- 423 [1] R. E. Horton, "The role of infiltration in the hydrologic cycle," *Trans. Amer. Geophys. Union*
424 **14**, 446–460 (1933).
- 425 [2] J. R. Philip, "Theory of infiltration," in *Advances in Hydroscience*, edited by V. T. Chow
426 (Academic Press, New York, 1969) pp. 215–296.
- 427 [3] D. E Hill and J.-Y. Parlange, "Wetting front instability in layered soils," *Soil Sci. Soc. Am.*
428 **J.** **36**, 697–702 (1972).
- 429 [4] L. Cueto-Felgueroso and R. Juanes, "Nonlocal interface dynamics and pattern formation
430 in gravity-driven unsaturated flow through porous media," *Phys. Rev. Lett.* **101**, 244504,
431 doi:10.1103/PhysRevLett.101.244504 (2008).
- 432 [5] A. Porporato, P. D'Odorico, F. Laio, L. Ridolfi, and I. Rodriguez-Iturbe, "Ecohydrology of
433 water-controlled ecosystems," *Adv. Water Resour.* **25**, 1335–1348 (2002).
- 434 [6] A. Porporato, E. Daly, and I. Rodriguez-Iturbe, "Soil water balance and ecosystem response
435 to climate change," *Am. Nat.* **164**, 625–632 (2004).
- 436 [7] D. deB. Richter and M. L. Mobley, "Monitoring Earth's critical zone," *Science* **326**, 1067–
437 1068 (2009).
- 438 [8] T. H. Illangasekare, J. L. Ramsey, K. H. Jensen, and M. B. Butts, "Experimental study
439 of movement and distribution of dense organic contaminants in heterogeneous aquifers," *J.*
440 *Contaminant Hydrol.* **20**, 1–25 (1995).
- 441 [9] K. D. Pennell, G. A. Pope, and L. M. Abriola, "Influence of viscous and buoyancy forces
442 on the mobilization of residual tetrachloroethylene during surfactant flushing," *Environ. Sci.*
443 *Technol.* **30**, 1328–1335 (1996).
- 444 [10] S. Bachu, W. D. Gunther, and E. H. Perkins, "Aquifer disposal of CO₂: Hydrodynamic and
445 mineral trapping," *Energy Conv. Manag.* **35**, 269–279 (1994).
- 446 [11] K. S. Lackner, "A guide to CO₂ sequestration," *Science* **300**, 1677–1678 (2003).
- 447 [12] F. M. Orr, Jr., "Storage of carbon dioxide in geologic formations," *J. Pet. Technol.* **56**, 90–97
448 (2004).
- 449 [13] IPCC, *Special Report on Carbon Dioxide Capture and Storage*, B. Metz et al. (eds.) (Cam-
450 bridge University Press, 2005).

- 451 [14] S. Bachu, "CO₂ storage in geological media: Role, means, status and barriers to deployment,"
452 Prog. Energy Combust. Sci. **34**, 254–273 (2008).
- 453 [15] M. L. Szulczewski, C. W. MacMinn, H. J. Herzog, and R. Juanes, "Lifetime of carbon capture
454 and storage as a climate-change mitigation technology," Proc. Natl. Acad. Sci. U.S.A. **109**,
455 5185–5189, doi:10.1073/pnas.1115347109 (2012).
- 456 [16] F. M. Orr, Jr. and J. J. Taber, "Use of carbon dioxide in enhanced oil recovery," Science
457 **224**, 563–569 (1984).
- 458 [17] L. W. Lake, *Enhanced Oil Recovery* (Prentice-Hall, Englewood Cliffs, NJ, 1989).
- 459 [18] L. Cueto-Felgueroso and R. Juanes, "Forecasting long-term gas production from shale," Proc.
460 Natl. Acad. Sci. U.S.A. **110**, 19660–19661, doi:10.1073/pnas.1319578110 (2013).
- 461 [19] N. Shakhova, I. Semiletov, A. Salyuk, V. Yusupov, D. Kosmach, and Ö. Gustafsson, "Exten-
462 sive methane venting to the atmosphere from sediments of the East Siberian Arctic shelf,"
463 Science **327**, 1246–1250 (2010).
- 464 [20] D. Bastviken, L. J. Tranvik, J. A. Downing, P. M. Crill, and A. Enrich-Prast, "Freshwater
465 methane emissions offset the continental carbon sink," Science **331**, 50 (2011).
- 466 [21] A. Skarke, C. Ruppel, M. Kodis, D. Brothers, and E. Lobecker, "Widespread methane
467 leakage from the sea floor on the northern US Atlantic margin," Nature Geoscience **7**, 657
468 (2014).
- 469 [22] C. Ruppel and J. D. Kessler, "The interaction of climate change and methane hydrates,"
470 Rev. Geophys. **55**, 126–168 (2017).
- 471 [23] C. Y. Wang, "Fundamental models for fuel cell engineering," Chem. Rev. **104**, 4727–4766
472 (2004).
- 473 [24] C. Lee, B. Zhao, R. Abouatallah, R. Wang, and A. Bazylak, "Compressible-gas invasion into
474 liquid-saturated porous media: application to polymer-electrolyte-membrane electrolyzers,"
475 Phys. Rev. Applied **11**, 054029 (2019).
- 476 [25] H. A. Stone, A. D. Stroock, and A. Ajdari, "Engineering flows in small devices: Microfluidics
477 toward a lab-on-a-chip," Annu. Rev. Fluid Mech. **36**, 381–411 (2004).
- 478 [26] A. A. Darhuber and S. M. Troian, "Principles of microfluidic actuation by modulation of
479 surface stresses," Annu. Rev. Fluid Mech. **37**, 425–455 (2005).
- 480 [27] G. M. Whitesides, "The origins and the future of microfluidics," Nature **442**, 368–373 (2006).

- 481 [28] H.-W. Lu, K. Glasner, A. L. Bertozzi, and C.-J. Kim, “A diffuse-interface model for elec-
482 trowetting drops in a Hele-Shaw cell,” *J. Fluid Mech.* **590**, 411–435 (2007).
- 483 [29] W. Song, T. W. de Haas, H. Fadaei, and D. Sinton, “Chip-off-the-old-rock: the study of
484 reservoir-relevant geological processes with real-rock micromodels,” *Lab Chip* **14**, 4382–4390
485 (2014).
- 486 [30] M. L. Porter, J. Jiménez-Martínez, R. Martinez, Q. McCulloch, J. W. Carey, and H. S.
487 Viswanathan, “Geo-material microfluidics at reservoir conditions for subsurface energy re-
488 source applications,” *Lab Chip* **15**, 4044–4053 (2015).
- 489 [31] W. Song and A. R. Kovscek, “Functionalization of micromodels with kaolinite for investiga-
490 tion of low salinity oil-recovery processes,” *Lab Chip* **15**, 3314–3325 (2015).
- 491 [32] S. A. Kelly, C. Torres-Verdin, and M. T. Balhoff, “Subsurface to substrate: dual-scale
492 micro/nanofluidic networks for investigating transport anomalies in tight porous media,”
493 *Lab Chip* **16**, 2829–2839 (2016).
- 494 [33] S. M. Prakadan, A. K. Shalek, and D. A. Weitz, “Scaling by shrinking: empowering single-
495 cell’omics’ with microfluidic devices,” *Nat. Rev. Genetics* **18**, 345–361 (2017).
- 496 [34] N. Chakrapani, B. Wei, A. Carrillo, P. M. Ajayan, and R. S. Kane, “Capillarity-driven
497 assembly of two-dimensional cellular carbon nanotube foams,” *Proc. Natl. Acad. Sci. U.S.A.*
498 **101**, 4009–4012 (2004).
- 499 [35] W. Wang, J. V. I. Timonen, A. Carlson, D.-M. Drotlef, C. T. Zhang, S. Kolle, A. Grinthal, T.-
500 S. Wong, B. Hatton, S. H. Kang, S. Kennedy, J. Chi, R. T. Blough, M. Sitti, L. Mahadevan,
501 and J. Aizenberg, “Multifunctional ferrofluid-infused surfaces with reconfigurable multiscale
502 topography,” *Nature* **559**, 77–82 (2018).
- 503 [36] D. J. Hornbaker, R. Albert, I. Albert, A.-L. Barabási, and P. Schiffer, “What keeps sand-
504 castles standing?” *Nature* **387**, 765–765 (1997).
- 505 [37] A. Groisman and E. Kaplan, “An experimental study of cracking induced by desiccation,”
506 *Europhys. Lett.* **25**, 415–420 (1994).
- 507 [38] H. Shin and J. C. Santamarina, “Fluid-driven fractures in uncemented sediments: Underlying
508 particle-level processes,” *Earth Planet. Sci. Lett.* **299**, 180–189 (2010).
- 509 [39] H. J. Cho, N. B. Lu, M. P. Howard, R. A. Adams, and S. S. Datta, “Crack formation and
510 self-closing in shrinkable, granular packings,” *Soft matter* **15**, 4689–4702 (2019).

- 511 [40] B. Sandnes, H. A. Knudsen, K. J. Måløy, and E. G. Flekkøy, “Labyrinth patterns in confined
512 granular-fluid systems,” Phys. Rev. Lett. **99**, 038001 (2007).
- 513 [41] B. Sandnes, E.G. Flekkøy, H.A. Knudsen, K. J. Måløy, and H. See, “Patterns and flow in
514 frictional fluid dynamics,” Nat. Commun. **2**, 288 (2011).
- 515 [42] A. Parmigiani, S. Faroughi, C. Huber, O. Bachmann, and Y. Su, “Bubble accumulation
516 and its role in the evolution of magma reservoirs in the upper crust,” Nature **532**, 492–495
517 (2016).
- 518 [43] R. Weinberger, “Initiation and growth of cracks during desiccation of stratified muddy sedi-
519 ments,” J. Struct. Geol. **21**, 379–386 (1999).
- 520 [44] B. Zhao, C. W. MacMinn, M. L. Szulczewski, J. A. Neufeld, H. E. Huppert, and R. Juanes,
521 “Interface pinning of immiscible gravity-exchange flows in porous media,” Phys. Rev. E **87**,
522 023015, doi:10.1103/PhysRevE.87.023015 (2013).
- 523 [45] P.-G. de Gennes, F. Brochard-Wyart, and D. Quéré, *Capillarity and Wetting Phenomena:
524 Drops, Bubbles, Pearls, Waves* (Springer, New York, 2004).
- 525 [46] R. Lenormand, C. Zarcone, and A. Sarr, “Mechanisms of the displacement of one fluid by
526 another in a network of capillary ducts,” J. Fluid Mech. **135**, 337–353 (1983).
- 527 [47] W. B. Haines, “Studies in the physical properties of soils. V. The hysteresis effect in capillary
528 properties, and the modes of moisture redistribution associated therewith,” J. Agr. Sci. **20**,
529 97–116 (1930).
- 530 [48] J. G. Roof, “Snap-off of oil droplets in water-wet pores,” Soc. Pet. Eng. J. **10**, 85–90 (1970).
- 531 [49] F. Moebius and D. Or, “Interfacial jumps and pressure bursts during fluid displacement in
532 interacting irregular capillaries,” J. Colloid Interface Sci. **377**, 406–415 (2012).
- 533 [50] R. T. Armstrong and S. Berg, “Interfacial velocities and capillary pressure gradients during
534 Haines jumps,” Phys. Rev. E **88**, 043010 (2013).
- 535 [51] S. Berg, H. Ott, S. A. Klapp, A. Schwing, R. Neiteler, N. Brussee, A. Makurat, L. Leu,
536 F. Enzmann, J.-O. Schwarz, M. Kersten, S. Irvine, and M. Stampanoni, “Real-time 3D
537 imaging of Haines jumps in porous media flow,” Proc. Natl. Acad. Sci. U.S.A. **110**, 3755–
538 3759 (2013).
- 539 [52] K. J. Måløy, L. Furberg, J. Feder, and T. Jøssang, “Dynamics of slow drainage in porous
540 media,” Phys. Rev. Lett. **68**, 2161–2164 (1992).

- 541 [53] L. Furuberg, K. J. Måløy, and J. Feder, “Intermittent behavior in slow drainage,” *Phys.*
542 *Rev. E* **53**, 966–977 (1996).
- 543 [54] R. Chandler, J. Koplik, K. Lerman, and J. F. Willemsen, “Capillary displacement and
544 percolation in porous media,” *J. Fluid Mech.* **119**, 249–267 (1982).
- 545 [55] D. Wilkinson and J. Willemsen, “Invasion percolation: a new form of percolation theory,” *J.*
546 *Phys. A* **16**, 3365–3376 (1983).
- 547 [56] R. Lenormand and C. Zarcone, “Invasion percolation in an etched network: measurement of
548 a fractal dimension,” *Phys. Rev. Lett.* **54**, 2226–2229 (1985).
- 549 [57] R. Lenormand, E. Touboul, and C. Zarcone, “Numerical models and experiments on immis-
550 cible displacements in porous media,” *J. Fluid Mech.* **189**, 165–187 (1988).
- 551 [58] R. Lenormand, “Liquids in porous media,” *J. Phys.: Condens. Matter* **2**, SA79–SA88 (1990).
- 552 [59] L. Paterson, “Diffusion-limited aggregation and two-fluid displacements in porous media,”
553 *Phys. Rev. Lett.* **52**, 1621–1624 (1984).
- 554 [60] K. J. Måløy, J. Feder, and T. Jøssang, “Viscous fingering fractals in porous media,” *Phys.*
555 *Rev. Lett.* **55**, 2688–2691 (1985).
- 556 [61] J.-D. Chen and D. Wilkinson, “Pore-scale viscous fingering in porous media,” *Phys. Rev.*
557 *Lett.* **55**, 1892–1895 (1985).
- 558 [62] J.-D. Chen, “Radial viscous fingering patterns in Hele-Shaw cells,” *Exp. Fluids* **5**, 363–371
559 (1987).
- 560 [63] S. Bryant and M. J. Blunt, “Prediction of relative permeability in simple porous media,”
561 *Phys. Rev. A* **46**, 2004–2011 (1992).
- 562 [64] E. Aker, K. J. Måløy, and A. Hansen, “Simulating temporal evolution of pressure in two-
563 phase flow in porous media,” *Phys. Rev. E* **58**, 2217–2226 (1998).
- 564 [65] E. Aker, K. J. Måløy, A. Hansen, and G. G. Batrouni, “A two-dimensional network simulator
565 for two-phase flow in porous media,” *Transp. Porous Media* **32**, 163–186 (1998).
- 566 [66] M. J. Blunt, “Flow in porous media—pore network models and multiphase flow,” *Curr. Opin.*
567 *Colloid Interface Sci.* **6**, 197–207 (2001).
- 568 [67] M. J. Blunt, M. D. Jackson, M. Piri, and P. H. Valvatne, “Detailed physics, predictive
569 capabilities and macroscopic consequences for pore-network models of multiphase flow,” *Adv.*
570 *Water Resour.* **25**, 1069–1089 (2003).

- 571 [68] M. S. Al-Gharbi and M. J. Blunt, “Dynamic network modeling of two-phase drainage in
572 porous media,” *Phys. Rev. E* **71**, DOI: 10.1103/PhysRevE.71.016308 (2005).
- 573 [69] V. Joekar-Niasar, S. M. Hassanzadeh, and H. K. Dahle, “Non-equilibrium effects in cap-
574 illarity and interfacial area in two-phase flow: dynamic pore-network modelling,” *J. Fluid
575 Mech.* **655**, 38–71 (2010).
- 576 [70] V. Joekar-Niasar and S. M. Hassanzadeh, “Analysis of fundamentals of two-phase flow in
577 porous media using dynamic pore-network models: a review,” *Crit. Rev. Environ. Sci. Tech-
578 nol.* **42**, 1895–1976 (2012).
- 579 [71] M. A. Gjennestad, M. Vassvik, S. Kjelstrup, and A. Hansen, “Stable and efficient time
580 integration of a dynamic pore network model for two-phase flow in porous media,” *Frontiers
581 Phys.* **6**, 56 (2018).
- 582 [72] B. Primkulov, S. Talman, K. Khaleghi, A. R. Shokri, R. Chalaturnyk, B. Zhao, C. W.
583 MacMinn, and R. Juanes, “Quasi-static fluid-fluid displacement in porous media: Invasion-
584 percolation through a wetting transition,” *Phys. Rev. Fluids* **3**, 104001 (2018).
- 585 [73] B. K. Primkulov, A. A. Pahlavan, X. Fu, B. Zhao, C. W. MacMinn, and R. Juanes, “Sig-
586 natures of fluid-fluid displacement in porous media: wettability, patterns, and pressures,” *J.
587 Fluid Mech.* **875**, R4 (2019).
- 588 [74] H. T. Kennedy, E. O. Burja, and R. S. Boykin, “An investigation of the effects of wettability
589 on the recovery of oil by water flooding,” *J. Physical Chem.* **59**, 867–869 (1955).
- 590 [75] P. P. Jadhunandan and N. R. Morrow, “Effect of wettability on waterflood recovery for
591 crude-oil/brine/rock systems,” *SPE Reserv. Eng.* **10**, 40–46 (1995).
- 592 [76] A. Seethepalli, B. Adibhatla, and K. K. Mohanty, “Physicochemical interactions during
593 surfactant flooding of fractured carbonate reservoirs,” *Soc. Pet. Eng. J.* **9**, 411–418 (2004).
- 594 [77] N. Morrow and J. Buckley, “Improved oil recovery by low salinity waterflooding,” *JPT* **63**,
595 106–112 (2011).
- 596 [78] G. Sharma and K. K. Mohanty, “Wettability alteration in high-temperature and high-salinity
597 carbonate reservoirs,” *Soc. Pet. Eng. J.* **18**, 646–655 (2013).
- 598 [79] M. Alava, M. Dubé, and M. Rost, “Imbibition in disordered media,” *Adv. Phys.* **53**, 83–175
599 (2004).
- 600 [80] A. Hernández-Machado, J. Soriano, A. M. Lacasta, M. A. Rodriguez, L. Ramírez-Piscina,
601 and J. Ortín, “Interface roughening in Hele-Shaw flows with quenched disorder: Experimental

602 and theoretical results," *Europhys. Lett.* **55**, 194–200 (2001).

603 [81] R. Planet, S. Santucci, and J. Ortín, "Avalanches and non-gaussian fluctuations of the global
604 velocity of imbibition fronts," *Phys. Rev. Lett.* **102**, 094502 (2009).

605 [82] X. Clotet, J. Ortín, and S. Santucci, "Disorder-induced capillary bursts control intermittency
606 in slow imbibition," *Phys. Rev. Lett.* **113**, 074501 (2014).

607 [83] M. Cieplak and M. O. Robbins, "Dynamical transition in quasistatic fluid invasion in porous
608 media," *Phys. Rev. Lett.* **60**, 2042–2045 (1988).

609 [84] M. Cieplak and M. O. Robbins, "Influence of contact angle on quasistatic fluid invasion of
610 porous media," *Phys. Rev. B* **41**, 11508–11521 (1990).

611 [85] P. E. Øren, S. Bakke, and O. J. Arntzen, "Extending predictive capabilities to network
612 models," *Soc. Pet. Eng. J.* **3**, 324–336 (1998).

613 [86] T. W. Patzek, "Verification of a complete pore network simulator of drainage and imbibition,"
614 *Soc. Pet. Eng. J.* **6**, 144–156 (2001).

615 [87] P. H. Valvatne and M. J. Blunt, "Predictive pore-scale modeling of two-phase flow in mixed
616 wet media," *Water Resour. Res.* **40**, W07406 (2004).

617 [88] E. J. Spiteri, R. Juanes, M. J. Blunt, and F. M. Orr, Jr., "A new model of trapping and
618 relative permeability hysteresis for all wettability characteristics," *Soc. Pet. Eng. J.* **13**, 277–
619 288, doi:10.2118/96448-PA (2008).

620 [89] K. Singh, M. Jung, M. Brinkmann, and R. Seemann, "Capillary-dominated fluid displace-
621 ment in porous media," *Annu. Rev. Fluid Mech.* **51**, 429–449 (2019).

622 [90] M. Trojer, M. L. Szulczewski, and R. Juanes, "Stabilizing fluid-fluid displace-
623 ments in porous media through wettability alteration," *Phys. Rev. Applied* **3**, 054008,
624 doi:10.1103/PhysRevApplied.3.054008 (2015).

625 [91] B. Zhao, C. W. MacMinn, and R. Juanes, "Wettability control on multiphase
626 flow in patterned microfluidics," *Proc. Natl. Acad. Sci. U.S.A.* **113**, 10251–10256,
627 doi:10.1073/pnas.1603387113 (2016).

628 [92] R. Holtzman and E. Segre, "Wettability stabilizes fluid invasion into porous media via non-
629 local, cooperative pore filling," *Phys. Rev. Lett.* **115**, 164501 (2015).

630 [93] B. Levaché, A. Azioune, M. Bourrel, V. Studer, and D. Bartolo, "Engineering the surface
631 properties of microfluidic stickers," *Lab Chip* **12**, 3028–3031 (2012).

- 632 [94] B. K. Primkulov, A. A. Pahlavan, X. Fu, B. Zhao, C. W. MacMinn, and R. Juanes, “Wet-
633 tability and Lenormand’s diagram,” (2020), submitted for publication.
- 634 [95] B. Zhao, C. W. MacMinn, B. K. Primkulov, Y. Chen, A. J. Valocchi, J. Zhao, Q. Kang,
635 K. Bruning, J. E. McClure, C. T. Miller, A. Fakhari, D. Bolster, T. Hiller, M. Brinkmann,
636 L. Cueto-Felgueroso, D. A. Cogswell, R. Verma, M. Prodanović, J. Maes, S. Geiger,
637 M. Vassvik, A. Hansen, E. Segre, R. Holtzman, Z. Yang, C. Yuan, B. Chareyre, and
638 R. Juanes, “Comprehensive comparison of pore-scale models for multiphase flow in porous
639 media,” *Proc. Natl. Acad. Sci. U.S.A.* **120**, 13799–13806 (2019).
- 640 [96] F. M. Orr, L. E. Scriven, and A. P. Rivas, “Pendular rings between solids: meniscus prop-
641 erties and capillary force,” *J. Fluid Mech.* **67**, 723–742 (1975).
- 642 [97] A. T. Skjeltorp and P. Meakin, “Fracture in microsphere monolayers studied by experiment
643 and computer simulation,” *Nature* **335**, 424–426 (1988).
- 644 [98] P. Meakin, “Models for material failure and deformation,” *Science* **252**, 226–234 (1991).
- 645 [99] J. Aizenberg, P. V. Braun, and P. Wiltzius, “Patterned colloidal deposition controlled by
646 electrostatic and capillary forces,” *Phys. Rev. Lett.* **84**, 2997–3000 (2000).
- 647 [100] M. Scheel, R. Seemann, M. Brinkmann, M. Di Michiel, A. Sheppard, B. Breidenbach, and
648 S. Herminghaus, “Morphological clues to wet granular pile stability,” *Nature Mat.* **7**, 189–193
649 (2008).
- 650 [101] J. A. Cartwright, “Episodic basin-wide fluid expulsion from geopressured shale sequences in
651 the North Sea basin,” *Geology* **22**, 447–450 (1994).
- 652 [102] K. Andreassen, A. Hubbard, M. Winsborrow, H. Patton, S. Vadakkepuliyambatta, A. Plaza-
653 Faverola, E. Gudlaugsson, P. Serov, A. Deryabin, R. Mattingsdal, *et al.*, “Massive blow-out
654 craters formed by hydrate-controlled methane expulsion from the arctic seafloor,” *Science*
655 **356**, 948–953 (2017).
- 656 [103] A. E. Lobkovsky, B. Jensen, A. Kudrolli, and D. H. Rothman, “Threshold phenomena in
657 erosion driven by subsurface flow,” *J. Geophys. Res.* **109**, F04010 (2004).
- 658 [104] D. M. Abrams, A. E. Lobkovsky, A. P. Petroff, K. M. Straub, B. McElroy, D. C. Mohrig,
659 A. Kudrolli, and D. H. Rothman, “Growth laws for channel networks incised by groundwater
660 flow,” *Nature Geosci.* **2**, 193–196 (2009).
- 661 [105] P. J. van den Hoek, G. M. M. Hertogh, A. P. Kooijman, Ph. de Bree, C. J. Kenter, and
662 E. Papamichos, “A new concept of sand production prediction: theory and laboratory ex-

663 periments," *SPE Drill. Complet.* **15**, 261–273 (2000).

664 [106] M. K. Hubbert and D. G. Willis, "Mechanics of hydraulic fracturing," *Petrol. Trans. AIME*
665 **210**, 153–163 (1957).

666 [107] E. Detournay, "Mechanics of hydraulic fractures," *Annu. Rev. Fluid Mech.* **48**, 311–339
667 (2016).

668 [108] H. Van Damme, F. Obrecht, P. Levitz, L. Gatineau, and C. Laroche, "Fractal viscous
669 fingering in clay slurries," *Nature* **320**, 731–733 (1986).

670 [109] E. Lemaire, P. Levitz, G. Daccord, and H. Van Damme, "From viscous fingering to vis-
671 coelastic fracturing in colloidal fluids," *Phys. Rev. Lett.* **67**, 2009–2012 (1991).

672 [110] C. W. MacMinn, E. R. Dufresne, and J. S. Wettlaufer, "Fluid-driven deformation of a soft
673 granular material," *Phys. Rev. X* **5**, 011020 (2015).

674 [111] A. K. Jain and R. Juanes, "Preferential mode of gas invasion in sediments: grain-scale
675 mechanistic model of coupled multiphase fluid flow and sediment mechanics," *J. Geophys.
676 Res.* **114**, B08101, doi:10.1029/2008JB006002 (2009).

677 [112] R. Holtzman, M. L. Szulczewski, and R. Juanes, "Capillary fracturing in granular media,"
678 *Phys. Rev. Lett.* **108**, 264504, doi:10.1103/PhysRevLett.108.264504 (2012).

679 [113] C. Peco, W. Chen, Y. Liu, M. M. Bandi, J. E. Dolbow, and E. Fried, "Influence of sur-
680 face tension in the surfactant-driven fracture of closely-packed particulate monolayers," *Soft
681 Matter* **13**, 5832–5841 (2017).

682 [114] W. S. Holbrook, H. Hoskins, W. T. Wood, R. A. Stephen, and D. Lizarralde, "Methane
683 hydrate and free gas on the Blake Ridge from vertical seismic profiling," *Science* **273**, 1840–
684 1842 (1996).

685 [115] J. R. Boles, J. F. Clark, I. Leifer, and L. Washburn, "Temporal variation in natural methane
686 seep rate due to tides, Coal Oil Point area, California," *J. Geophys. Res.* **106**, 27077–27086
687 (2001).

688 [116] K. U. Heeschen, A. M. Trehu, R. W. Collier, E. Suess, and G. Rehder, "Distribution and
689 height of methane bubble plumes on the Cascadia Margin characterized by acoustic imaging,"
690 *Geophys. Res. Lett.* **30**, 1643, doi:10.1029/2003GL016974 (2003).

691 [117] E. A. Solomon, M. Kastner, I. R. MacDonald, and I. Leifer, "Considerable methane fluxes
692 to the atmosphere from hydrocarbon seeps in the Gulf of Mexico," *Nat. Geosci.* **2**, 561–565
693 (2009).

- 694 [118] N. L. B. Bangs, M. J. Hornbach, and C. Berndt, "The mechanics of intermittent methane
695 venting at South Hydrate Ridge inferred from 4D seismic surveying," *Earth Planet. Sci. Lett.*
696 **310**, 105–112 (2011).
- 697 [119] C. S. Martens and J. Val Klump, "Biogeochemical cycling in an organic-rich coastal marine
698 basin. 1. Methane sediment-water exchange processes," *Geochim. Cosmochim. Acta* **44**, 471–
699 490 (1980).
- 700 [120] J. P. Chanton and C. S. Martens, "Seasonal variations in ebullitive flux and carbon isotopic
701 composition of methane in a tidal freshwater estuary," *Glob. Biogeochem. Cycle* **2**, 289–298
702 (1988).
- 703 [121] J. Greinert, D. F. McGinnis, L. Naudts, P. Linke, and M. De Batist, "Atmospheric methane
704 flux from bubbling seeps: Spatially extrapolated quantification from a Black Sea shelf area,"
705 *J. Geophys. Res.* **115**, C01002 (2010).
- 706 [122] C. Varadharajan, R. Hermosillo, and H. F. Hemond, "A low-cost automated trap to measure
707 bubbling gas fluxes," *Limnol. Oceanogr. Methods* **8**, 363–375 (2010).
- 708 [123] B. P. Scandella, L. Pillsbury, T. Weber, C. Ruppel, H. Hemond, and R. Juanes, "Ephemer-
709 ality of discrete methane vents in lake sediments," *Geophys. Res. Lett.* **43**, 4374–4381,
710 doi:10.1002/2016GL068668 (2016).
- 711 [124] T. Delsontro, D. F. McGinnis, S. Sobek, I. Ostrovsky, and B. Wehrli, "Extreme methane
712 emissions from a Swiss hydropower reservoir: Contribution from bubbling sediments," *Env-
713 iron. Sci. Technol.* **44**, 2419–2425 (2010).
- 714 [125] P. B. Flemings, X. Liu, and W. J. Winters, "Critical pressure and multiphase flow in Blake
715 Ridge gas hydrates," *Geology* **31**, 1057–1060 (2003).
- 716 [126] X. Liu and P. B. Flemings, "Passing gas through the hydrate stability zone at southern
717 Hydrate Ridge, offshore Oregon," *Earth Planet. Sci. Lett.* **241**, 211–216 (2006).
- 718 [127] X.-Z. Kong, W. Kinzelbach, and F. Stauffer, "Migration of air channels: An instability of
719 air flow in mobile saturated porous media," *Chem. Eng. Sci.* **64**, 1528–1535 (2009).
- 720 [128] X.-Z. Kong, W. Kinzelbach, and F. Stauffer, "Morphodynamics during air injection into
721 water-saturated movable spherical granulates," *Chem. Eng. Sci.* **65**, 4652–4660 (2010).
- 722 [129] G. Varas, V. Vidal, and J.-C. Géminard, "Morphology of air invasion in an immersed granular
723 layer," *Phys. Rev. E* **83**, 061302 (2011).

- 724 [130] G. Varas, V. Vidal, and J.-C. Géminard, “Venting dynamics of an immersed granular layer,”
 725 Phys. Rev. E **83**, 011302 (2011).
- 726 [131] A. Islam, S. Chevalier, I. Ben Salem, Y. Bernabe, R. Juanes, and M. Sassi, “Characterization
 727 of the crossover from capillary invasion to viscous fingering to fracturing during drainage in
 728 a vertical 2D porous medium,” Int. J. Multiphase Flow **58**, 279–291 (2014).
- 729 [132] S. Lee, J. Lee, R. Le Mestre, F. Xu, and C. W. MacMinn, “Migration, trapping, and venting
 730 of gas in a soft granular material,” arXiv preprint arXiv:1808.02921v3 (2020).
- 731 [133] G. Varas, V. Vidal, and J.-C. Géminard, “Dynamics of crater formations in immersed
 732 granular materials,” Phys. Rev. E **79**, 021301 (2009).
- 733 [134] B. P. Scandella, K. Delwiche, H. Hemond, and R. Juanes, “Persistence of bub-
 734 ble outlets in soft, methane-generating sediments,” J. Geophys. Res. **122**, 1298–1320,
 735 doi:10.1002/2016jg003717 (2017).
- 736 [135] Z. Sun and J. C. Santamarina, “Grain-displacive gas migration in fine-grained sediments,”
 737 J. Geophys. Res. **124**, 2274–2285 (2019).
- 738 [136] M. J. Dalbe and R. Juanes, “Morphodynamics of fluid–fluid displacement in 3d deformable
 739 granular media,” Phys. Rev. Applied **9**, 024028 (2018).
- 740 [137] J.-M. Konrad and R. Ayad, “Desiccation of a sensitive clay: field experimental observations,”
 741 Canad. Geotech. J. **34**, 929–942 (1997).
- 742 [138] L. Pauchard, V. Lazarus, B. Abou, K. Sekimoto, G. Aitken, and C. Lahanier, “Craquelures
 743 dans les couches picturales des peintures d’art,” Reflets Phys. **3**, 5–9 (2007).
- 744 [139] M. Leang, F. Giorgiutti-Dauphine, L.-T. Lee, and L. Pauchard, “Crack opening: from
 745 colloidal systems to paintings,” Soft Matter **13**, 5802–5808 (2017).
- 746 [140] L. Goehring, A. Nakahara, T. Dutta, S. Kitsunezaki, and S. Tarafdar, *Desiccation Cracks
 747 and Their Patterns: Formation and Modelling in Science and Nature* (John Wiley & Sons,
 748 2015).
- 749 [141] L. Xu, S. Davies, A. B. Schofield, and D. A. Weitz, “Dynamics of drying in 3D porous
 750 media,” Phys. Rev. Lett. **101**, 094502 (2008).
- 751 [142] E. R. Dufresne, E. I. Corwin, N. A. Greenblatt, J. Ashmore, D. Y. Wang, A. D. Dinsmore,
 752 J. X. Cheng, X. S. Xie, J. W. Hutchinson, and D. A. Weitz, “Flow and fracture in drying
 753 nanoparticle suspensions,” Phys. Rev. Lett. **91**, 224501 (2003).

- 754 [143] L. Goehring, W. J. Clegg, and A. F. Routh, “Plasticity and fracture in drying colloidal
755 films,” *Phys. Rev. Lett.* **110**, 024301 (2013).
- 756 [144] K. A. Shorlin, J. R. de Bruyn, M. Graham, and S. W. Morris, “Development and geometry
757 of isotropic and directional shrinkage-crack patterns,” *Phys. Rev. E* **61**, 6950–6957 (2000).
- 758 [145] T. Hornig, I. M. Sokolov, and A. Blumen, “Patterns and scaling in surface fragmentation
759 processes,” *Phys. Rev. E* **54**, 4293–4298 (1996).
- 760 [146] S. Kitsunezaki, “Fracture patterns induced by desiccation in a thin layer,” *Phys. Rev. E* **60**,
761 6449–6464 (1999).
- 762 [147] K. t. Leung and Z. Néda, “Pattern formation and selection in quasistatic fracture,” *Phys.*
763 *Rev. Lett.* **85**, 662–665 (2000).
- 764 [148] H. Shin and J. C. Santamarina, “Desiccation cracks in saturated fine-grained soils: particle-
765 level phenomena and effective-stress analysis,” *Geotechnique* **61**, 961–972 (2011).
- 766 [149] T. Cajuhi, L. Sanavia, and L. De Lorenzis, “Phase-field modeling of fracture in variably
767 saturated porous media,” *Comp. Mech.* **61**, 299–318 (2018).
- 768 [150] T. Hu, J. Guilleminot, and J. E. Dolbow, “A phase-field model of fracture with frictionless
769 contact and random fracture properties: Application to thin-film fracture and soil desicca-
770 tion,” *Comput. Methods Appl. Mech. Engrg.* **368**, 113106 (2020).
- 771 [151] H. J. Cho and S. S. Datta, “Scaling law for cracking in shrinkable granular packings,” *Phys.*
772 *Rev. Lett.* **123**, 158004 (2019).
- 773 [152] P. G. Saffman and G. I. Taylor, “The penetration of a fluid into a porous medium or Hele-
774 Shaw cell containing a more viscous liquid,” *Proc. R. Soc. London Ser. A* **245**, 312–329
775 (1958).
- 776 [153] B. Sandnes, E.G. Flekkøy, and K. J. Måløy, “Stick slip displacement of confined granular
777 mixtures: Bubble expansion,” *Eur. Phys. J. Special Topics* **204**, 19–25 (2012).
- 778 [154] F. K. Eriksen, R. Toussaint, K.-J. Måløy, E. G. Flekkøy, O. Galland, and B. Sandnes,
779 “Pattern formation of frictional fingers in a gravitational potential,” *Phys. Rev. Fluids* **3**,
780 013801 (2018).
- 781 [155] R. Toussaint, G. Løvoll, Y. Méheust, K. J. Måløy, and J. Schmittbuhl, “Influence of pore-
782 scale disorder on viscous fingering during drainage,” *Europhys. Lett.* **71**, 583–589 (2005).
- 783 [156] R. Holtzman and R. Juanes, “Crossover from fingering to fracturing in deformable disordered
784 media,” *Phys. Rev. E* **82**, 046305, doi:10.1103/PhysRevE.82.046305 (2010).

- 785 [157] F. K. Eriksen, R. Toussaint, K.-J. Måløy, and E. G. Flekkøy, “Invasion patterns during
786 two-phase flow in deformable porous media,” *Frontiers in Physics* **3**, 81 (2015).
- 787 [158] C. Chevalier, A. Lindner, M. Leroux, and E. Clement, “The instability of slow, immiscible,
788 viscous liquid-liquid displacements in permeable media,” *J. Non-Newton. Fluid Mech.* **158**,
789 63–72 (2009).
- 790 [159] H. Huang, F. Zhang, P. Callahan, and J. Ayoub, “Granular fingering in fluid injection into
791 dense granular media in a Hele-Shaw cell,” *Phys. Rev. Lett.* **108**, 258001 (2012).
- 792 [160] M. Trojer, P. de Anna, and R. Juanes, “Impact of wetting on fracturing of granular media,”
793 (2020), submitted for publication.
- 794 [161] Y. Meng, B. K. Primkulov, Z. Yang, C. Y. Kwok, and R. Juanes, “Jamming transition and
795 emergence of fracturing in wet granular media,” *Phys. Rev. Research* **2**, 022012(R) (2020).
- 796 [162] ITASCA, *PFC2D, v3.1 – Theory and Background*, Itasca Consulting Group, Inc., Minneapolis,
797 MN (2004).
- 798 [163] P. A. Cundall and O. D. L. Strack, “Discrete numerical model for granular assemblies,”
799 *Geotechnique* **29**, 47–65 (1979).
- 800 [164] T. S. Majmudar, M. Sperl, S. Luding, and R. P. Behringer, “Jamming transition in granular
801 systems,” *Phys. Rev. Lett.* **98**, 058001 (2007).
- 802 [165] C. Heussinger and J.-L. Barrat, “Jamming transition as probed by quasistatic shear flow,”
803 *Phys. Rev. Lett.* **102**, 218303 (2009).
- 804 [166] A. J. Liu and S. R. Nagel, “Nonlinear dynamics: Jamming is not just cool any more,” *Nature*
805 **396**, 21–22 (1998).
- 806 [167] M. Moura, K. J. Måløy, and R. Toussaint, “Critical behavior in porous media,” *Europhys.
807 Lett.* **118**, 14004 (2017).
- 808 [168] C. Odier, B. Levaché, E. Santanach-Carreras, and D. Bartolo, “Forced imbibition in porous
809 media: a fourfold scenario,” *Phys. Rev. Lett.* **119**, 208005 (2017).
- 810 [169] M. Saadatfar, A. P. Sheppard, T. J. Senden, and A. J. Kabla, “Mapping forces in a 3D
811 elastic assembly of grains,” *J. Mech. Phys. Solids* **60**, 55–66 (2012).
- 812 [170] N. Brodu, J. A. Dijksman, and R. P. Behringer, “Spanning the scales of granular materials
813 through microscopic force imaging,” *Nat. Comm.* **6**, 6361 (2015).
- 814 [171] R. C. Hurley, S. A. Hall, J. E. Andrade, and J. Wright, “Quantifying interparticle forces
815 and heterogeneity in 3D granular materials,” *Phys. Rev. Lett.* **117**, 098005 (2016).

- 816 [172] M. Frocht, *Photoelasticity* (John Wiley & Sons, 1941).
- 817 [173] T. S. Majmudar and R. P. Behringer, “Contact force measurements and stress-induced
818 anisotropy in granular materials,” *Nature* **435**, 1079–1082 (2005).
- 819 [174] K. E. Daniels, J. E. Kollmer, and J. G. Puckett, “Photoelastic force measurements in
820 granular materials,” *Rev. Sci. Instr.* **88**, 051808 (2017).
- 821 [175] N. Iikawa, M. M. Bandi, and H. Katsuragi, “Sensitivity of granular force chain orientation
822 to disorder-induced metastable relaxation,” *Phys. Rev. Lett.* **116**, 128001 (2016).
- 823 [176] S. Lherminier, R. Planet, G. Simon, L. Vanel, and O. Ramos, “Revealing the structure of a
824 granular medium through ballistic sound propagation,” *Phys. Rev. Lett.* **113**, 098001 (2014).
- 825 [177] S. Lherminier, R. Planet, V. Levy dit Vehel, G. Simon, L. Vanel, K. J. Måløy, and O. Ramos,
826 “Continuously sheared granular matter reproduces in detail seismicity laws,” *Phys. Rev. Lett.*
827 **122**, 218501 (2019).
- 828 [178] A. L. Handwerger, A. W. Rempel, R. M. Skarbek, J. J. Roering, and G. E. Hilley, “Rate-
829 weakening friction characterizes both slow sliding and catastrophic failure of landslides,”
830 *Proc. Natl. Acad. Sci. U.S.A.* **113**, 10281–10286 (2016).
- 831 [179] J. Palmer, “Creeping catastrophes—studies of slow landslides could unmask the mechanics
832 of a worldwide scourge,” *Nature* **548**, 384–386 (2017).
- 833 [180] C. H. Scholz, “Earthquakes and friction laws,” *Nature* **391**, 37–42 (1998).
- 834 [181] C. H. Scholz, *The mechanics of earthquakes and faulting*, 3rd ed. (Cambridge University
835 Press, 2019).
- 836 [182] Y. Jiang, G. Wang, and T. Kamai, “Acoustic emission signature of mechanical failure:
837 Insights from ring-shear friction experiments on granular materials,” *Geophys. Res. Lett.*
838 **44**, 2782–2791 (2017).
- 839 [183] M. J. Ikari, D. M. Saffer, and C. Marone, “Frictional and hydrologic properties of clay-rich
840 fault gouge,” *J. Geophys. Res.* **114**, B05409 (2009).
- 841 [184] M. Sawai, A. R. Niemeijer, O. Plümper, T. Hirose, and C. J. Spiers, “Nucleation of frictional
842 instability caused by fluid pressurization in subducted blueschist,” *Geophys. Res. Lett.* **43**,
843 2543–2551 (2016).
- 844 [185] M. M. Scuderi and C. Collettini, “The role of fluid pressure in induced vs. triggered seismicity:
845 Insights from rock deformation experiments on carbonates,” *Sci. Rep.* **6**, 24852 (2016).

- 846 [186] M. M. Scuderi, C. Collettini, and C. Marone, “Frictional stability and earthquake triggering
847 during fluid pressure stimulation of an experimental fault,” *Earth Planet. Sci. Lett.* **477**,
848 84–96 (2017).
- 849 [187] F. Cappa, M. M. Scuderi, C. Collettini, Y. Guglielmi, and J.-P. Avouac, “Stabilization of
850 fault slip by fluid injection in the laboratory and in situ,” *Science Advances* **5**, eaau4065
851 (2019).
- 852 [188] T. Xing, W. Zhu, M. French, and B. Belzer, “Stabilizing effect of high pore fluid pressure
853 on slip behaviors of gouge-bearing faults,” *J. Geophys. Res.* **124**, 9526–9545 (2019).
- 854 [189] M. F. Linker and J. H. Dieterich, “Effects of variable normal stress on rock friction: Observations
855 and constitutive equations,” *J. Geophys. Res.* **97**, 4923–4940 (1992).
- 856 [190] C. Marone, C. B. Raleigh, and C. H. Scholz, “Frictional behavior and constitutive modeling
857 of simulated fault gouge,” *J. Geophys. Res.* **95**, 7007–7025 (1990).
- 858 [191] Y. Guglielmi, F. Cappa, J.-P. Avouac, P. Henry, and D. Elsworth, “Seismicity triggered by
859 fluid injection-induced aseismic slip,” *Science* **348**, 1224–1226 (2015).